Diagenetic formation of stevensite by replacement of diatom frustules in the sediments of the alkaline Lake Alchichica (Mexico)

Elodie Muller, William Rapin, Jeanne Caumartin, Didier Jézéquel, Alexis de Wever, Christophe Thomazo, Robin Havas, Purificación López-García, David Moreira, Rozaluz Tavera, et al.

Diagenetic formation of stevensite by replacement of diatom frustules in the sediments of the alkaline Lake Alchichica (Mexico)

Elodie Muller[a], William Rapin[a,b], Jeanne Caumartin[a], Didier Jézéquel[c], Alexis De Wever[a], Christophe Thomazo[d,e], Robin Havas[d], Purificación López-García[f], David Moreira[f], Rozaluz Tavera[g], Karim Benzerara[a]*

[a]*Sorbonne Université, Muséum National d'Histoire Naturelle, UMR CNRS 7590, Institut de Minéralogie, de Physique des Matériaux et de Cosmochimie (IMPMC), 4 Place Jussieu, 75005 Paris, France*

[b]*IRAP, CNRS UMR 5277, OMP, Université de Toulouse, France*

[c]*IPGP, CNRS UMR 7154, Université de Paris & UMR CARRTEL, INRAE-USMB, France*

[d]*UMR CNRS/uB6282 Biogéosciences, Université de Bourgogne Franche-Comté, 6 Bd Gabriel, 21000 Dijon, France*

[e]*Institut Universitaire de France, Paris, France*

[f]*Ecologie, Systématique et Evolution, CNRS, Université Paris-Saclay, AgroParisTech, Orsay, France*

[g]*Departamento de Ecología y Recursos Naturales, Universidad Nacional Autónoma de México, DF México, Mexico*

*Corresponding author: karim.benzerara@upmc.fr

Abstract:

Better understanding the conditions of formation of authigenic Mg-silicates and their reactivity is key to interpret the paleoenvironmental message carried by the sedimentary record and evaluate the effect of reverse weathering, a process involved in long-term climate evolution. Microbialites from most alkaline crater lakes in Mexico contain Mg-silicates except those in Lake Alchichica, where concentration of orthosilicic acid is low (< 26 µM). Here, we investigated the first meter of sediments in Lake Alchichica in order to check how their mineralogy compared with that of shoreline microbialites. The mineralogy and chemistry of the sediment column were determined together with the pore water chemistry, providing insights on the processes occurring during early diagenesis. Below ~3 cm in depth, diatom frustules are progressively pseudomorphized into Al-poor Mg-silicates with a composition corresponding to

stevensite. This diagenetic process is massive and the resulting silicate represents between 30 and 53 wt.% of the sediment content at all depths. This observation questions the possibility to infer lake paleochemistry from the presence/absence of Mg-silicates in the sedimentary record. Moreover, it allowed us to refine the conditions under which Mg-silicates authigenesis occurs: the saturation of the solution should be higher or equal to the solubility of a Mg-silicate phase close to that of "amorphous sepiolite". Although the solubility of authigenic silicates is a key parameter of reverse weathering modeling during geological times, it is still debated. In this study, we proposed a solubility constant deduced from a natural system that should be considered when modelling the formation of Mg-silicates in a natural environment. The proportion of reverse weathering associated with this solubility constant could be higher than previously predicted based on experiments and thus have a greater impact on climate stability over geological timescales.

Keywords: reverse weathering; diatoms; Mg-silicates; solubility; diagenesis

A) Introduction

Authigenic clays are reported in various sedimentary environments from marine (*e.g.* Tosca et al., 2011) to soils (*e.g.* Cuadros et al., 2016), speleothems (*e.g.* Léveillé et al., 2002) and lacustrine environments (*e.g.* Deocampo, 2015; Wright and Barnett, 2015). They form either through direct precipitation from solution (*i.e.* neoformation) or by transformation of precursor minerals (also called neoformation by addition) (Jones, 1986; Galán and Pozo, 2011). In the sedimentary environment, transformation is mostly related to diagenesis, whereas neoformation can take place in both syngenetic (depositional) and diagenetic environments (Galan and Pozo, 2011). Clays forming in evaporitic closed basins where parent rocks are enriched in

ferromagnesian minerals, tend to be Mg-rich minerals as reported in the American Great Salt Lake (Jones and Deocampo, 2005) and Lake Abert (Jones and Weir, 1983), in several modern East African lake basins (Jones, 1986; Deocampo, 2005, 2015) and in Mexican crater lakes (Zeyen et al., 2015). Hereafter, they are referred to as Mg-silicates (Jones, 1986). They constitute a significant part of the Mg-rich phyllosilicate family. They structurally and chemically encompass diverse phases, either rich in Al such as saponite and palygorskite or poor in Al such as sepiolite, stevensite and kerolite (Pozo and Calvo, 2018). The latter, not listed as a valid mineral species by the international mineralogical association, is considered as a stacking-disordered talc phase (Brindley et al., 1977)

Al-poor Mg-silicates have been extensively studied in modern lakes from different localities such as the Satonda crater lake (Indonesia; Arp et al., 2003; Benzerara et al., 2010), Eyasi and Ngorongoro Crater Lakes (Tanzania; Deocampo, 2005), Lake Van (eastern Anatolia; Reimer et al., 2009), Lake Clifton (western Australia; Burne et al., 2014), Atexcac, Quechulac and La Preciosa Lakes (Mexico; Zeyen et al., 2015), Dziani Dzaha Lake (Mayotte; Gérard et al., 2018, Milesi et al., 2019, 2020), Mono Lake and Great Salt Lake (USA; Souza-Egipsy et al., 2005; Pace et al., 2016), as well as peri-marine environments (*e.g.* Léveillé et al., 2000a, 2000b; Warren, 2016). Last but not least, such authigenic Mg-silicate phases have been observed in some ancient marine and lacustrine formations showing that they can be traced back in the geological record. For example, Tosca et al. (2011) reported occurrences of talc in two early Neoproterozoic carbonate formations located in the Akademikerbreen Group (Svalbard) and in the upper Fifteenmile Group of the Ogilvie Mountains (NW Canada), which they interpreted as the product of dehydration of authigenic hydrous Mg-silicates, including kerolite. It has been shown that the identity of these phases in modern environments depends on specific geochemical factors, such as pH, dissolved CO_2, salinity, alkalinity, dissolved element

concentration ratios, and the activities of Mg^{2+}, H_4SiO_4, Al^{3+}, Ca^{2+}, and Fe^{3+} in solution (Jones and Galán, 1988; Weaver, 1989; Deocampo, 2005; Bristow and Milliken, 2011). Several experimental studies have investigated the conditions allowing their formation (*e.g.* Wollast et al., 1968; Tosca et al., 2011). They have shown that high pH > 8.2 and high concentrations of Si and/or Mg are required for their precipitation (Zeyen et al., 2015; Tosca et al., 2011). In addition, high salinity favors the formation of stevensite, whereas sepiolite and kerolite are formed under lower saline conditions, with high Si/Mg ratio favoring the formation of sepiolite. Likewise, precipitation of kerolite instead of sepiolite is favored by an increase of pH and dissolved Mg concentration (Pozo and Calvo, 2018). Last, Millot et al. (1970) proposed that the Al content of Mg-silicates could be indicative of the distance to the detrital source. Millot's model shows that detrital clay inputs, mainly kaolinite, illite, chlorite and Al-rich smectite preferentially occur in the margins of saline lake basins and transition to fibrous clays (palygorskite, sepiolite) that precipitate in the center of lakes.

Overall, these minerals have received considerable attention as potential paleoenvironmental recorders of the geochemistry of the solution in which they precipitated. In addition to their value for paleoenvironmental reconstruction, better understanding the conditions of Mg-silicates formation and their reactivity is interesting for two broad questions. First, they can have a crucial role in the control of carbonate fabrics and porosity as exemplified by the study of offshore Barra Velha Formation carbonate reservoirs in Brazil (Tosca and Wright, 2018; Wright and Barnett, 2020). Second, their precipitation feeds a process called reverse weathering, which consumes alkalinity without consuming carbon and may therefore have a significant role in the evolution of climates at the geological timescale (Krissansen-Totton and Catling, 2020; Isson and Planavsky, 2018). However, there remains a few difficulties for their use as a proxy. First, there is some uncertainty about the exact value of the

106 solubility constant of the amorphous Mg-silicates, commonly considered as precursors to the
107 formation of Mg-silicates in laboratory experiments (i.e. sepiolite, kerolite, stevensite; e.g.
108 Tosca et al., 2011). Second, Mg-silicates may form either in the water column or in sediments
109 during early diagenesis (Işik Ece, 1998; Bristow et al. 2009; Milesi et al. 2019, 2020). In the
110 latter case, they do not reflect the chemistry of the waters in the depositional basin but instead
111 that in the sediment pore waters. Moreover, several authors have suggested that some
112 biogeochemical processes may trigger Mg-silicate formation, possibly obscuring the
113 relationship between the identity and presence/absence of Mg-silicates and bulk chemical
114 conditions. For instance, recent studies reported Mg-silicates formed by a local pH increase
115 and/or nucleation on extracellular polymeric substances within microbial mats, acting as
116 precursors of carbonate precipitation in microbialites (Bontognali et al., 2010; Burne et al.,
117 2014; Zeyen et al., 2015; Pace et al., 2016). The association of Mg-silicates and biofilms has
118 also been evidenced in certain speleothems (Melim and Spilde, 2018), mostly in volcanic caves
119 (Léveillé et al., 2002; Miller et al., 2014). In some cases, Mg-silicates were shown to develop
120 at the surface of diatom frustules (Badaut and Risacher, 1983; Bentz and Peterson, 2020). Yet,
121 although Mg-silicates have shown a strong potential for fossilization of microbes and organic
122 matter (Zeyen et al., 2015), the role of the microorganisms in the formation of these phases
123 remains unclear.
124
125 Mg-silicates, characterized as poorly crystalline hydrated talc phases similar to kerolite,
126 were reported in shallow microbialites from numerous alkaline crater lakes in Mexico (*e.g.*
127 Atexcac, La Preciosa, Quechulac; Zeyen et al., 2015, 2021). By contrast, the shallow
128 microbialites of the Mexican Lake Alchichica were essentially composed of hydromagnesite
129 and aragonite, but did not contain kerolite, possibly because lake water had a low concentration
130 in orthosilicic acid (< 26 μM). Here, we investigated deep sediments in Lake Alchichica in

order to check how their mineralogy compared with that of shoreline microbialites. The mineralogy and chemistry of the first meter of the sediment column were studied together with the pore water chemistry providing insights on the processes occurring during early diagenesis.

B) Geological Setting

Alchichica is a crater lake located in the eastern part of the trans-Mexican volcanic belt (TMVB) in the Cuenca de Oriental region (19°24'N and 97°24'W; **Figure 1a**). The TMVB is a seismically and volcanically active zone resulting from the subduction of the Rivera and Cocos plates beneath North America at the Middle American Trench during the Neogene period (Ferrari et al., 2012). It is composed of diverse volcanic structures formed on a basement predominately composed of highly folded and faulted Cretaceous limestones and shales as well as small plutonic intrusions of granodiorite, monzonite, and syenite emplaced during the Oligocene and the Miocene (Negendank et al., 1985). These basement rocks are covered by Miocene to Pleistocene andesitic rocks, which are themselves overlain by (i) widespread pyroclastic deposits derived from both local phreatomagmatic volcanoes and large eruptions from nearby volcanoes, as well as (ii) lacustrine deposits. The crater of Alchichica is surrounded by an asymmetric ring of tephra, deposited by several Hawaiian, strombolian and phreatomagmatic eruptions dated from >114 ka to 6.3 ± 5.1 ka by $^{40}Ar/^{39}Ar$ methods (Tchamabé et al., 2020). The crater rim is mainly composed of maar deposits (i.e. pyroclastic rocks including 44 to 73 wt.% of juvenile clasts) and basaltic andesite lava flow and scoriaceous pre-maar deposits outcropping only on the west side of the crater (**Figure 1**; Tchamabé et al., 2020).

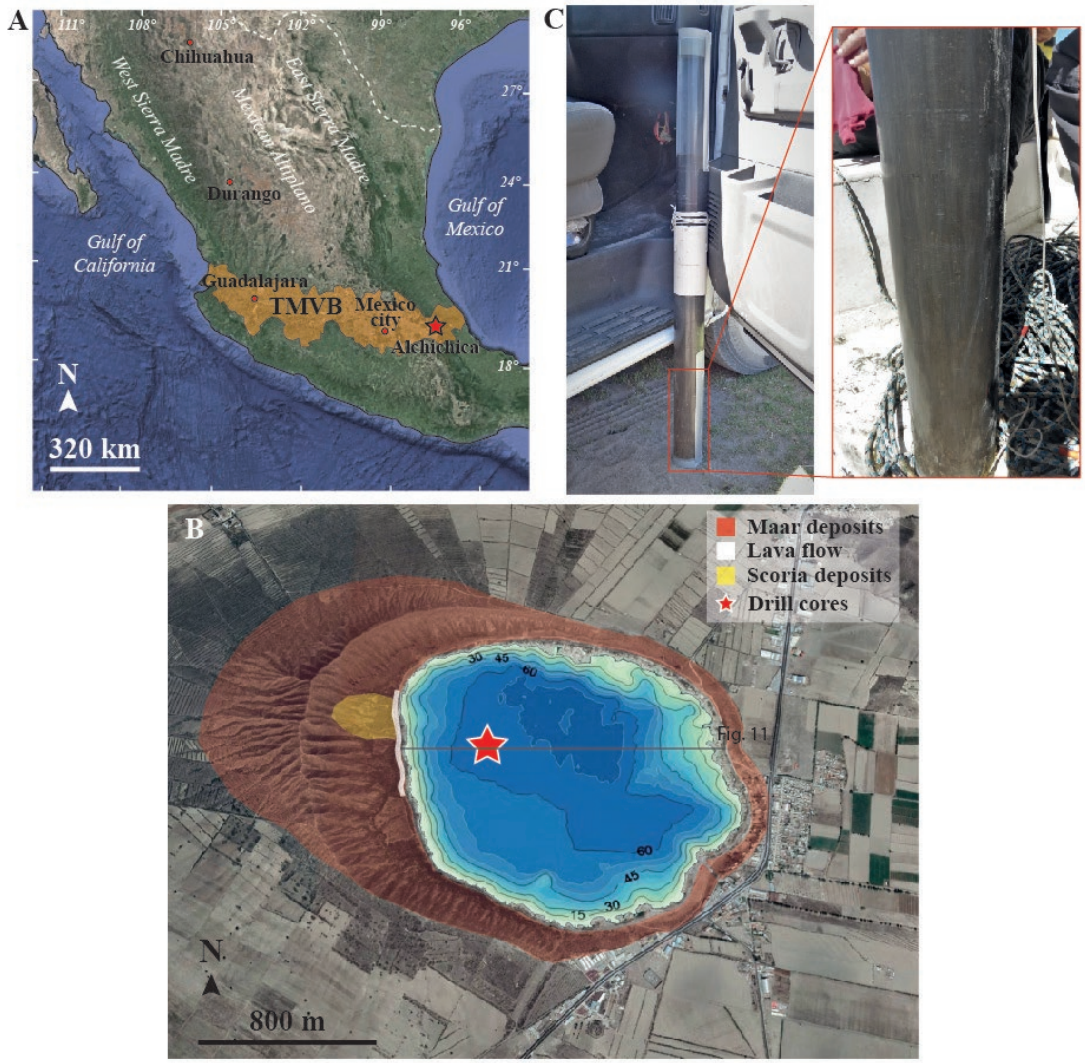

Figure 1: A) Relief map of Mexico representing the location of the lake Alchichica in the trans-Mexican volcanic belt (TMVB, orange area, modified from (Ferrari et al. 2012)); B) Google Earth image of Lake Alchichica showing the surrounding volcanic deposits (from Tchamabé et al., 2020), bathymetrical data (from Alcocer & Oseguera, 2019) and the location of the drill core (red star). C) Pictures of the 85.5 cm long sediment core.

With a maximum depth of 65 m (Arredondo-Figueroa et al., 1983; Vilaclara et al., 1993), Alchichica is the deepest crater lake in Mexico. It is located at 2,320 m a.s.l. on a high-altitude plateau called Los Llanos de San Juan. The climate is semi-arid with an annual precipitation regime of less than 400 mm and an annual evaporation rate of about 1700 mm (Alcocer, 2021). The air temperature seasonally ranges from -5.5 to 30°C (Alcocer and Hammer, 1998). The lake is supplied by rainfall and groundwaters as suggested by Armienta et al. (2008) for all maar lakes. The water deficit between evaporation and rainfall could be partially balanced by

underground sources and outflows (García Martínez, 2010), yet the lake water level has decreased to a rate of about 8 $cm.yr^{-1}$ for several decades (Alcocer, 2021). Water in Lake Alchichica is alkaline (pH>9), subsaline (~7.9 g/L) and dominated by Na^+, Cl^-, HCO_3^- and Mg^{2+} ions. Two main factors control its chemical composition: 1) the weathering of surrounding bedrocks (basalts and Cretaceous limestones) through groundwater supply and 2) the evaporation of the lake due to the semi-arid climate (Zeyen et al., 2021). Alchichica is a monomictic lake stratified during most of the year and homogenized during winter (Arredondo-Figueroa, 2002). Two annual blooms of primary producers were observed by previous studies: a diatom bloom during the winter mixing (December-January) and a cyanobacteria bloom at the onset of the stratification period (April-May) (Alcocer et al., 2000; Vilaclara et al., 1993). Microbialites were extensively studied in Lake Alchichica and are mainly composed of hydromagnesite and aragonite in varying proportions (Kazmierczak et al., 2011; Couradeau et al., 2011, 2013; Gérard et al., 2013; Saghaï et al., 2015; Valdespino-Castillo et al., 2018; Zeyen et al., 2021). They are covered by complex microbial communities dominated by oxygenic and anoxygenic photosynthesizers (Couradeau et al., 2011; Saghaï et al., 2016; Iniesto et al., 2021).

C) Material and Methods

a. Sample collection

Lake water was sampled with a Niskin bottle in May 2019 in the center of the lake at 0, 5, 10, 20, 30, 40, 50, 55 and 60 m depth. Temperature, pH and salinity were measured *in situ* with a YSI Exo 2 multi-parameter probe. Hundreds of milliliters of solution were systematically filtered using 0.22 µm Filtropur S filters. For major cation analysis, 30 mL of solution were acidified with nitric acid (2%). One hundred and thirty milliliters were used for measurements of anion and orthosilicic acid (H_4SiO_4) concentrations, without pre-acidification. For dissolved

195 inorganic carbon (DIC) analysis, 12 mL were placed in airtight Labco Exetainer® tubes in order
196 to avoid exchange of DIC with atmospheric CO_2.
197
198 The sediment core was collected from the bottom of the lake at 61 m in depth during
199 the same field campaign in May 2019, using a gravitational Uwitec corer with a diameter of 90
200 mm. The total length of the recovered core was 85.5 cm (**Figure 1c**). The sediment core was
201 then cut in two in order to allow its processing in a glove-bag. The two cores were transferred
202 into a glove-bag and placed under anoxic conditions (N_2 atmosphere) immediately after
203 collection. They were then processed and split into cm-scale fractions along the core's vertical
204 axis. The porewater was separated from the solid phases once extracted from the core barrel
205 using Rhizon samplers connected via tubing to syringes (filtration to 0.2 μm). During all the
206 slicing process, oxygen levels were monitored with a Multi 3630 IDS WTW oxygen meter
207 (equipped with a FDO 925-3 O_2 optode) and were always below the detection limit of 0.1 mg/L.
208 The pH of the porewaters were measured (with a Sentix 940 IDS WTW electrode) immediately
209 after water collection within the glove-bag. Sediments were packaged under nitrogen and
210 transported in heat sealed airtight bags (PP016 H Protective Packaging Ltd) with O_2 trap
211 (Anaerocult® A), then fully dried in an anoxic N_2-filled glove box in the lab.
212
213 **b. Chemical analyses of solutions**
214
215 Chemical analyses for major elements (Al, B, Ca, K, Li, Mg, Na, Mn, Si, S, Cl) are
216 summarized in **Table 1**. They were carried out at the Laboratoire Géoscience Océan (UBO,
217 Brest, France) using inductively coupled plasma-atomic emission spectroscopy (ICP-AES).
218 Anion concentrations (F^-, Cl^-, Br^-, and SO_4^{2-}) were measured by ion chromatography and
219 orthosilicic acid (H_4SiO_4) concentrations were determined by continuous flow colorimetric

analyses at the Institut de physique du globe de Paris (IPGP, Paris, France). The uncertainty on the concentration measurements of cations, anions and orthosilicic acid was lower than ± 5%.

Dissolved inorganic carbon (DIC) concentrations were determined at the IPGP, using an "Analytical Precision 2003" Gas Chromatograph – Isotope Ratio Mass Spectrometer (running under He-continuous flow) following the analytical protocol detailed in Assayag et al. (2006). An aliquot of the water sample was injected into a Labco Exetainer® tube pre-loaded with H_3PO_4 and He. After the dissolved CO_2 has equilibrated with the head-space gas (for one night), gases (i.e. He and CO_2) were sampled and quantified with the GC-IRMS by comparison with internal standards of known concentrations. Each measurement represents an average of four injections in the mass spectrometer and all samples were duplicated (including chemical preparation and analysis). Standard deviation for [DIC] is 1 mM (n=33), on average.

Activities of cations, anions and orthosilicic acid as well as saturation indices of the solutions were calculated using the software PHREEQC 3 (Parkhurst and Appelo, 2013) and the thermodynamic database "thermoddem.dat" (Blanc et al., 2012).

c. Bulk analyses of sediments

A quantity of about 10 g for each sediment sample was finely ground and homogenized in an agate mortar and aliquots of the same powdered sample were used for the different bulk analyses.

X-ray powder diffraction

For X-ray diffraction (XRD) analyses, each core sample powder was placed onto 3 cm diameter sample holders and leveled to form a flat surface for analysis. XRD analyses were performed using a Panalytical Xpert Pro transmission diffractometer with a cobalt anode

operated at 45 kV and 40 mA and a slit of 0.5° at 240 mm radius distance. The 2θ scan was performed in the continuous mode from 4° to 110° (2θ) with a step of 0.024°.

Each diffractogram was corrected for small relative displacements of sample height using the alignment with major aragonite diffraction peaks (2θ-Co angles 30.52° and 53.77°), dominant in all samples. The background signal was fit so that the contribution of X-ray low crystalline phases could be removed from peak analysis. Automatic background determination did not produce adequate results given the presence of magnesium silicate and opaline silica in the sample generating broad diffraction signals, but these were used to assess the relative presence of the two low crystalline materials (**Figure S1**). The background signal was manually fit with an interpolated spline for each diffractogram. Peak identification was performed using pattern search on the X-ray diffraction database of reference spectra "Crystallography Open Database (COD)" (from http://www.crystallography.net/).

Structural data of identified minerals were obtained from the crystallography open database (COD). The structure and abundance of crystalline minerals were estimated using a Rietveld refinement analysis implemented in the Highscore Plus software (**Figure S2**). XRD identifications were cross-checked back and forth with results from energy dispersive X-ray spectrometry (EDXS) elemental composition data obtained by scanning electron microscopy (SEM) to more confidently identify the mineralogy of (core) samples.

Fourier transform infrared spectroscopy analyses

For attenuated total reflectance (ATR) - Fourier transform infrared (FTIR) spectroscopy analyses, ~1 mg of sediment powder was pressed against a single-reflection diamond prism. ATR spectra were recorded between 400 and 4000 cm^{-1} with a resolution of 1 cm^{-1}, using a Nicolet 6700 FTIR spectrometer equipped with a deuterated triglycine sulfate (DTGS) detector. Spectra were corrected from the atmospheric signal.

Bulk chemical analyses of sediments

Concentrations of major elements were measured on 30 sediment samples using an ICP-AES ICap 6500 (Thermo Fischer) after alkali fusion of rock samples with $LiBO_2$ followed by dissolution in HNO_3 at the Service d'Analyse des Roches et Minéraux (SARM, Centre de Recherches Pétrographiques et Géochimiques, Nancy, France). About two grams of ground powder were used for these analyses. The uncertainties on the major element measurements, between 1 and 25% depending on their concentrations, were assessed from relative standard deviations calculated on a minimum of 30 measurements of reference geochemical standards.

Microscopy analyses of sediments

Around 5 mm^3 of powder (<100 µm) from 8 samples (at 0.5, 2, 4, 8.5, 37.3, 41.5, 44.5 and 84.8 cm) collected all along the core length were progressively impregnated in hard grade LR-white resin (Polysciences, Inc.) by incubating them at 6°C for 18 h in (1:2) then (2:1) mixture of LR-white/ethanol and finally in pure LR-white resin. After 1 h at room temperature, the resin was polymerized by incubation at 40°C for 1 h and at 60°C for 24 h. Once polymerization was completed, inclusions were polished with diamond polishing paper with a grain size down to a ¼ of a micrometer and rinsed in deionized water with ultrasounds for 10 minutes. Scanning electron microscopy (SEM) analyses were performed using a Zeiss Ultra 55 field emission gun (FEG) SEM. Backscattered electron (BSE) images were acquired using an angle selective backscattered (AsB) detector at an accelerating voltage of 15 kV, a working distance of ~7.5 mm and a 60 mm aperture at high current. The elemental composition of mineral phases was determined by energy dispersive X-ray spectrometry (EDXS) using an EDS QUANTAX detector after copper calibration. Semi-quantification of the spectra was achieved using the ESPRIT software package (Bruker) and the phi-rho-z method.

An electron-transparent foil (~100 nm in thickness) was cut by focused ion beam (FIB) milling from one of the embedded samples, to further analyze by transmission electron microscopy (TEM) a diatom replaced by Mg-silicates (at 16-19 cm in depth). This was performed at IMPMC using a Zeiss Crossbeam Neon40. We used the lift-out procedure as described by Benzerara et al. (2005). A FIB-assisted Pt deposit was first made. A 30 kV Ga+ beam operated at ~5 nA was then used for initial milling, resulting in rough excavation from both sides of the thin foil. An *in situ* micromanipulator was attached to the foil by FIB-assisted platinum deposition prior to separation of the foil (at ~100 pA). The thin foil was transferred to a TEM grid and welded to it. Further thinning of the foil was performed with the beam operated at a low, ~100 pA current. A last cleaning step was performed at low acceleration tension (~3 kV).

The electron-transparent foil was then analyzed by TEM using a JEOL 2100F operating at 200 kV and equipped with a field emission gun (FEG-TEM). Scanning transmission electron microscopy (STEM) observations were performed in the high-angle annular dark field mode (HAADF) and a probe size of 1 nm. EDXS mapping was performed using the STEM mode.

D) Results

Solution chemistry of the water column and the sediment pore water

Solutions at all depths in the water column of Lake Alchichica are dominated by sodium, chloride and magnesium (**Figure 2; Table 1**). In the water column, the temperature decreases from 19.5 to 15.2°C with depth and the chemical composition remains stable, with a pH of 9.2 and concentrations of DIC at 33.9 mM, Mg at 18.8 mM and Ca at 0.1 mM (**Figure 2; Table 1**). The concentration of orthosilicic acid in the water column is below the detection limit (0.1 µM)

from the surface down to 30 m in depth, then increases to 26 µM at 60 m (maximum depth of the lake). In the sediments, pore waters are also dominated by sodium, chloride and magnesium (**Figure 2; Table 1**). The [Mg] decreases in the first 20 centimeters from 18.1 to 15.2 mM and then remains constant with a peak at 17.1 mM at 34.5-40 cm depth. The pH also decreases down to 8.47 in the first ten centimeters of the sediments and then remains constant. The concentration of orthosilicic acid in porewater is significantly higher than in the lake water. It decreases from 760 µM at 0.5 cm down to 380 µM at 28-40 cm and raises again to 620 µM at 83 cm deep. The DIC concentration globally increases from the top to the bottom of the core, from 35.8 mM to 43.2 mM. The [Ca] varies non-monotonously between 0.09 and 0.14 mM (**Figure 2; Table 1**).

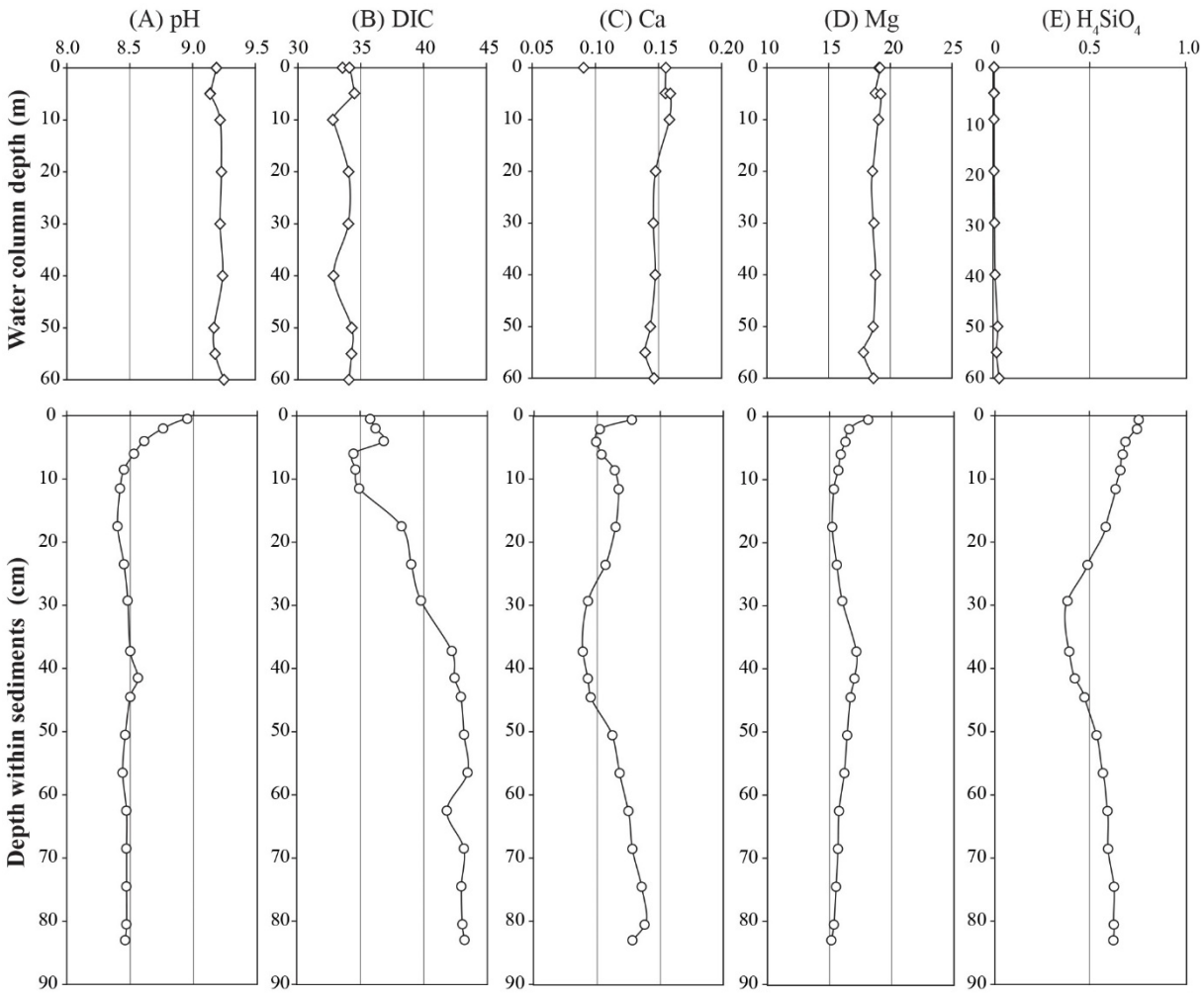

Figure 2: Depth profiles of (A) pH, (B) dissolved inorganic carbon (DIC), (C) Ca, (D) Mg and (E) H_4SiO_4 concentrations in mM along the water column (top part, diamonds) *versus* in porewater in the first 83 cm of sediments (bottom part, circles).

Table 1. pH, DIC and major element concentrations measured in lake and pore waters. Relative standard deviation is ≤5% for DIC and element concentrations and ±0.02 units for pH values. Charge balance (Bal.) in % is calculated as 100*(Σcations - Σanions)/((Σcations +Σanions)/2).

	Depth	pH	T	DIC	Cl	Na	Mg	SO_4^{2-}	K	B	Li	Ca	Mn	H_4SiO_4	Al	Bal.
			°C	mM	mM	mM	mM	mM	mM	mM	mM	mM	mM	mM	µM	%
Lake water																
AL19_0m-ext	0 m	9.19	19.6	34.1	116	108	19.1	12.8	4.96	3.79	0.35	0.16	<DL	<DL	<DL	-14.2
AL19_4.9m	4.9	9.14	19.2	34.5	107	106	18.8	11.8	4.91	3.79	0.35	0.16	<DL	<DL	0.96	-9.5
AL19_5m	5	9.14	19.2		107	108	19.3	11.9	5.01	3.84	0.35	0.16	<DL	<DL	<DL	-8.0
AL19_10m	10	9.22	19.2	32.8	106	107	19.1	11.8	5.00	3.83	0.35	0.16	<DL	<DL	<DL	-7.3
AL19_20m	20	9.23	16.7	34.0	106	105	18.6	11.8	4.90	3.75	0.34	0.15	<DL	<DL	<DL	-10.0
AL19_30m	30	9.22	15.5	34.0	106	105	18.7	11.7	4.90	3.75	0.34	0.15	<DL	0.002	<DL	-9.7
AL19_40m	40	9.24	15.3	32.8	106	106	18.8	11.8	4.87	3.74	0.35	0.15	<DL	0.005	<DL	-9.0
AL19_50m	50	9.17	15.2	34.3	108	104	18.7	12.0	4.82	3.75	0.34	0.14	<DL	0.018	<DL	-12.6
AL19_55m	55	9.18	15.2	34.3	109	100	17.9	12.0	4.62	3.58	0.32	0.14	<DL	0.013	<DL	-16.9
AL19_60m	60	9.25	15.2	34.1	112	104	18.7	12.2	4.84	3.75	0.34	0.15	<DL	0.026	<DL	-14.3
Sediment porewater																
AL19_C2a_0.5cm	0-1 cm	8.95	N.D.	35.8	97.4	109	18.1	9.92	5.05	3.85	0.35	0.13	0.02	0.76	2.01	2.4
AL19_C2a_2cm	1-3	8.76	N.D.	36.2	99.8	105	16.6	9.50	5.03	3.71	0.34	0.10	0.012	0.75	<DL	8
AL19_C2a_4cm	3-5	8.61	N.D.	36.8	99.0	106	16.3	9.21	5.03	3.74	0.34	0.10	0.012	0.69	<DL	5.9
AL19_C2a_6cm	5-7	8.53	N.D.	34.5	99.6	105	15.9	9.09	5.06	3.68	0.33	0.10	0.013	0.67	0.08	7.7
AL19_C2a_8.5cm	7-10	8.45	N.D.	34.6	100.2	104	15.7	8.70	5.06	3.72	0.33	0.11	0.022	0.66	1.16	8.1
AL19_C2a_11.5cm	10-13	8.42	N.D.	34.9	98.9	105	15.4	8.26	5.08	3.77	0.33	0.12	0.028	0.64	0.45	8.8
AL19_C2a_17.5cm	16-19	8.4	N.D.	38.2	98.2	103	15.2	8.06	5.02	3.71	0.32	0.11	0.036	0.59	0.47	10.2
AL19_C2a_23.5cm	22-25	8.45	N.D.	39.0	96.2	103	15.6	7.40	5.02	3.74	0.31	0.11	0.011	0.49	<DL	8.1
AL19_C2a_29.3cm	28-30.5	8.48	N.D.	39.8	94.6	100	16.0	7.00	4.96	3.68	0.30	0.09	0.011	0.38	<DL	9.1
AL19_C2a_37.3cm	34.5-40	8.5	N.D.	42.2	93.2	102	17.1	6.16	5.06	3.80	0.30	0.09	0.011	0.39	<DL	4.4
AL19_C2a_41.5cm	40-43	8.56	N.D.	42.4	94.4	100	17.0	5.56	4.93	3.62	0.29	0.09	0.011	0.42	<DL	6.1
AL19_C2b_44.5cm	43-46	8.5	N.D.	42.9	96.6	99.4	16.7	5.62	4.89	3.59	0.29	0.09	0.012	0.47	0.44	8.9
AL19_C2b_50.5cm	49-52	8.46	N.D.	43.2	97.2	99.4	16.4	5.47	4.87	3.57	0.28	0.11	0.012	0.54	0.34	9.6
AL19_C2b_56.5cm	55-58	8.44	N.D.	43.4	95.3	97.8	16.2	5.13	4.81	3.56	0.28	0.12	0.013	0.57	<DL	8.5
AL19_C2b_62.5cm	61-64	8.47	N.D.	41.8	95.4	97.0	15.8	4.84	4.79	3.52	0.27	0.12	0.013	0.59	0.27	10.2
AL19_C2b_68.5cm	67-70	8.47	N.D.	43.1	94.6	96.3	15.7	4.90	4.71	3.48	0.27	0.13	0.002	0.60	0.50	10.3
AL19_C2b_74.5cm	73-76	8.47	N.D.	43.0	96.7	96.2	15.5	4.49	4.74	3.50	0.26	0.14	0.002	0.63	0.71	11.4
AL19_C2b_80.5cm	79-82	8.47	N.D.	43.0	94.2	95.6	15.3	4.20	4.68	3.52	0.26	0.14	0.002	0.63	0.31	10.3
AL19_C2b_83cm	82-84	8.46	N.D.	43.2	93.8	95.9	15.1	4.09	4.65	3.48	0.26	0.13	0.002	0.62	0.03	2.1

Saturations of the solutions with respect to authigenic silicate and silica phases are best visualized in a diagram, where the logarithm of the $a(Mg^{2+})/a(H^+)^2$ activity ratio is plotted against the logarithm of the orthosilicic acid activity ($a(H_4SiO_4)$) (**Figure 3**). As the orthosilicic acid concentration increases with depth in the water column, the lake water reaches saturation with respect to several low-temperature Mg-silicates such as sepiolite, kerolite, talc and

stevensite below 30 m in depth. However, all lake waters down to 60 m remain undersaturated with respect to "amorphous sepiolite", as defined by Wollast et al. (1968). By contrast, all sediment pore solutions are saturated/supersaturated with respect to "amorphous sepiolite". Two trends can be detected: (1) from 0 to 11.5 cm in depth, pore waters align along a vertical trend, i.e. at a constant $a(H_4SiO_4)$, located between the solubility lines of quartz and amorphous silica (arrow 1 in **Figure 3**); (2) from 11.5 to 84.8 cm, pore waters follow a trend parallel to the "amorphous sepiolite" solubility line (arrow 2 in **Figure 3**). Only one sample of pore water from the top of the sediments (0-1 cm) lies above the critical supersaturation line for homogeneous nucleation of Mg-silicates as defined by Tosca et al. (2011) and Tosca and Masterson (2014).

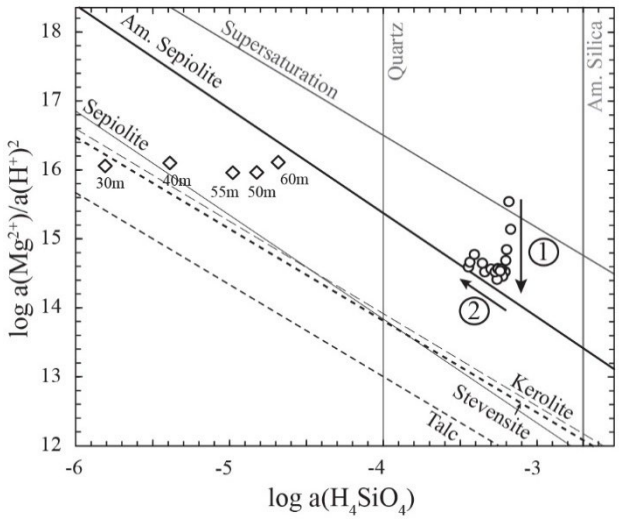

Figure 3: Solubility diagram in the $\log[a(Mg^{2+})/a(H^+)^2] - \log[a(H_4SiO_4)]$ space determined at 25°C. Lake (diamond) and pore waters (dots) of Alchichica are plotted against the solubility lines of talc (Jones and Galan, 1988), stevensite (Chahi et al., 1997), kerolite and sepiolite (Stoessell, 1988), amorphous sepiolite (Wollast et al., 1968), quartz and amorphous silica (Truesdell and Jones, 1974). The ''supersaturation" line results from experiments conducted by Tosca et al. (2011) and Tosca and Masterson (2014) and relates to homogeneous nucleation of Mg-silicate phases from solution. The arrows 1 and 2 show the main trends followed by Alchichica sediment pore waters respectively between 0 and 11.5 cm and between 11.5 and 84.8 cm. Above 30 m in the lake waters, silica is below the detection limit and hence data are not represented in this diagram.

Saturations of solutions with respect to several carbonate phases are visualized in other diagrams, where the logarithms of $a(Ca^{2+})$ or $a(Mg^{2+})$ are plotted against the log of $a(CO_3^{2-})$

(**Figure S3**). These diagrams clearly show that lake and pore waters are supersaturated with respect to calcite and aragonite at all depths but only lake waters reach saturation with monohydrocalcite (MHC; **Figure S3a**). The water column of Lake Alchichica is oversaturated at all depths with amorphous Mg carbonate (AMC) as defined by Fukushi and Matsumiya (2018) (**Figure S3b**) and therefore with hydromagnesite as well. All pore waters but those between 8.5 and 23.5 cm, are saturated or supersaturated with hydromagnesite.

Bulk mineralogy

X-ray diffraction analyses highlight that aragonite is the dominant mineral species in the sediments with an abundance varying between 40 and 80 wt.% (amorphous-free) as estimated by Rietveld (**Figures 4 and S4, Table S1).** Detrital silicate minerals (albite, bytownite, quartz and pigeonite) are also detected in all diffractograms, their total abundance varying from 15 to 60 wt.% (amorphous-free). The relative abundance of aragonite and detrital species are anticorrelated to some degree along the core, but other mineral phases exhibit key variations with depth. In particular, substantial amount of hydromagnesite is identified in the first two samples near the sediment surface (up to 15 wt.% in the top 3 cm of the core), but is absent at depth (< 1 wt.%) except within a specific interval near 35 cm in depth where hydromagnesite is clearly detected (~ 8 wt.%) along with huntite (~ 11 wt.%), a trigonal carbonate phase of formula $Mg_3Ca(CO_3)_4$. Poorly crystalline magnesium silicates and opaline silica can also be detected by XRD (**Figure S1**). The estimation of the intensity of the broad x-ray scattering signal related to silica reveals that it is most intense near surface but significantly decreases within the sediment below, with the lowest signal near 35 cm. By contrast, the magnesium silicate, identified as a kerolite or a stevensite based on broad diffraction peaks at 22.7°, 41.2° and 71.8° 2θ angles (see Zeyen et al., 2015 for more details about XRD

identification), is not detected in the first two samples at the surface but clearly detected deeper on, with a low relative intensity near 35 cm. Other minor minerals are detected by XRD in all samples, such as calcite (average abundance of 2.6 wt.% as suggested by Rietveld), and halite, which likely formed when the samples containing Cl-rich pore waters were dried.

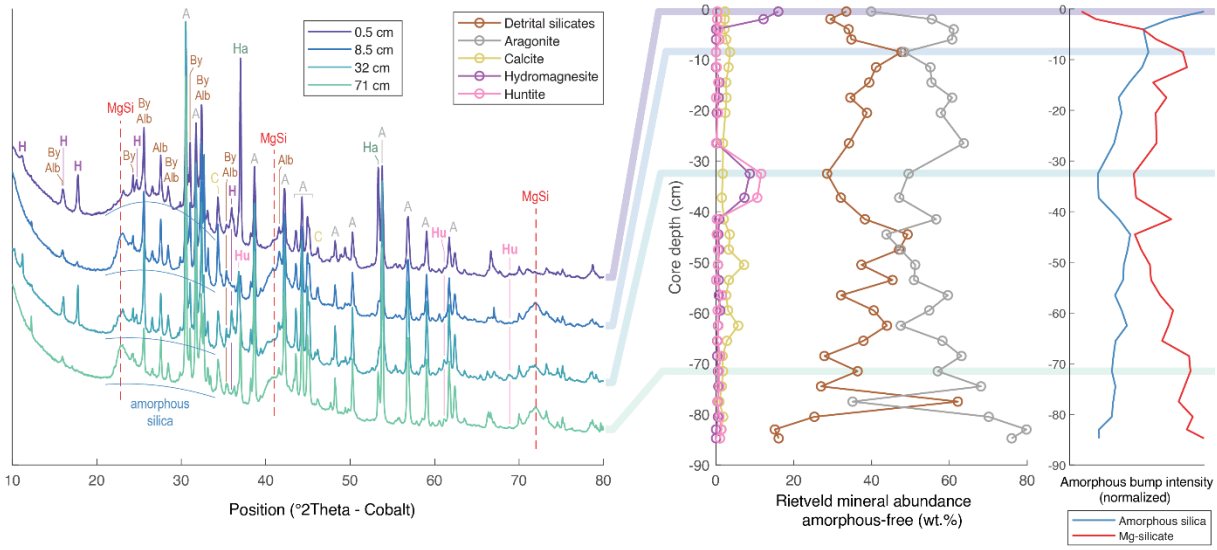

Figure 4: X-ray diffraction analyses of Alchichica sediment core samples. (Left panel) Selected diffraction patterns (at 0.5 cm, 8.5 cm, 32.5 cm and 71.5 cm depth) highlighting the key crystalline mineral assemblages used for Rietveld refinement analysis (A: aragonite, Alb: albite, By: bytownite, H: hydromagnesite, Hu: huntite, Ha: halite, C: calcite, see **Figure S4** for all patterns), along with the broad diffraction signals of poorly crystalline magnesium silicate (MgSi, kerolite or stevensite) and amorphous silica. (**Middle panel)** Estimated crystalline mineral relative abundances and (**Right panel)** relative intensity of XRD signals affiliated to poorly crystalline phases (see also **Figure S1**) in the core with depth.

FTIR analyses of the sediment samples show an evolution of their mineralogical composition with depth in perfect agreement with XRD analyses (**Figures 5, S4 and S5**). The aragonite signal is present in all samples at all depths (**Figure S5**), as attested by bands at 700, 713, 845, 855, 1083, 1464 and 1512 cm^{-1} (Zeyen et al., 2015). In surface sediment spectra (down to 10 cm), bands at 796, 1059 and 1230 cm^{-1}, characteristic of amorphous silica (Nied et al., 2015; d'Espinose de la Caillerie et al., 1995) are detected as well as bands at 887, 1420 et 1477 cm^{-1}, characteristic of hydromagnesite (Farmer, 1974). These bands disappear in deeper samples except for the 37.3 cm depth. By contrast, Mg-silicates (e.g., kerolite or stevensite) are

absent in surface samples but detected in FTIR spectra of all sediments deeper than 10 cm as shown by the presence of OH absorption bands at 662 and 670 cm^{-1} (Tosca & Masterson, 2014), Si-OH stretching band at 892 cm^{-1} and Si-O stretching band at 981 cm^{-1} (Zeyen et al., 2015). Only the sediment samples at 34.5-40 cm in depth appeared anomalous in that trend: in particular it notably shows the reappearance of hydromagnesite as attested by the bands at 887 and 1420 cm^{-1}, but also the presence of huntite as attested by the bands at 870, 878, 891, 1442, 1511 and 1551 cm^{-1} (Kangal et al., 2005, Hollingbery and Hull, 2012).

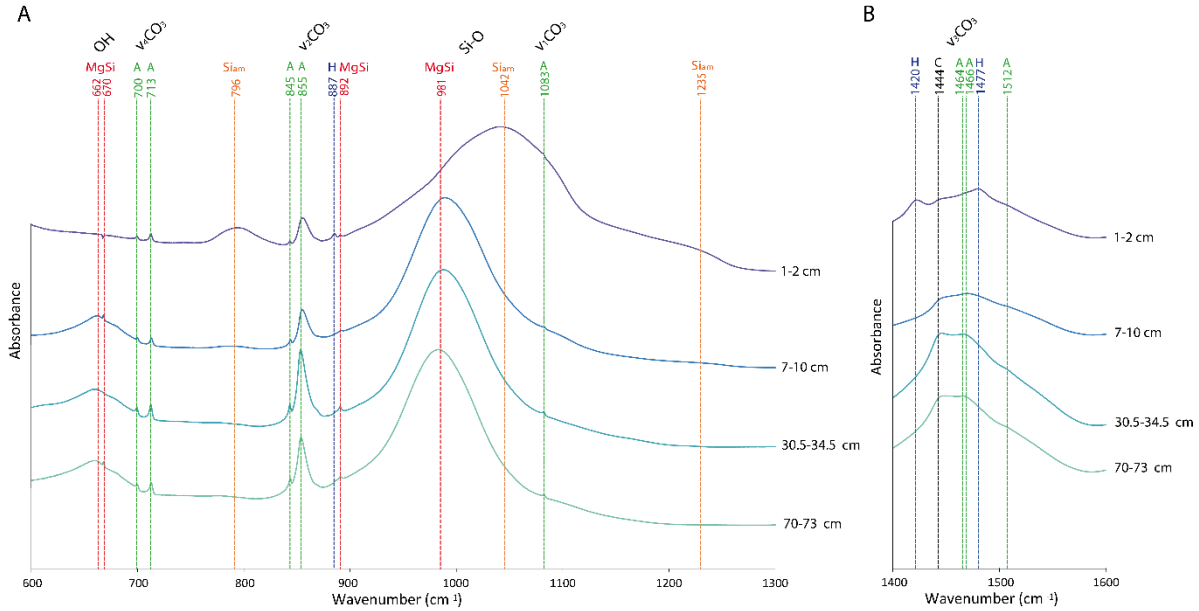

Figure 5: Selected FTIR spectra of Alchichica sediment samples (at increasing depth from top to bottom, same depths as those shown in Fig. 4). (A) Spectra in the 600 to 1300 cm^{-1} wavenumber range. (B) Spectra of the same samples from 1400 to 1600 cm^{-1}. The dashed lines show characteristic bands of silicates [red for authigenic magnesium silicates (MgSi), orange for amorphous silicates (Si_{am})] and carbonates [green for aragonite (A), black for calcite (C), blue for hydromagnesite (H)] in the samples.

Observations by scanning electron microscopy and EDXS analyses of 8 samples also confirm the evolution of the mineralogical composition of the sediments with depth in total agreement with FTIR and XRD data. SEM-EDXS analyses show that the sediments contain abundant fine-grained Ca-carbonates chemically consistent with aragonite at all depths. By

contrast, Mg-rich non-silicate minerals (containing Mg, O and C only) are detected only in the first ten centimeters of sediments and at 34.5-40 cm and likely correspond to hydromagnesite as supported by XRD and FTIR analyses (**Figure 6**). A Ca- and Mg-rich mineral interpreted as huntite based on a Mg/Ca ratio of about 3 is locally observed in samples C2a-05 (7-10 cm), C2a-10 (34.5-40 cm), C2a-11 (40-43 cm) and C2b-12 (43-46 cm). Huntite grains are relatively small, measuring less than 20 μm in size. Regarding Si-rich mineral phases, various grains are best interpreted as detrital minerals. The stoichiometry of these grains together with XRD analyses allowed to identify them as alkaline feldspars and quartz (**Table S2**). Other detrital minerals rich in Mg, Al, Si, and K show elemental Si/Al and Mg/Al ratios consistent with olivine and pyroxenes (**Table S2**). Last, SEM images show that diatom frustules are very abundant in the sediments at all depths, most of them are broken (and potentially degraded during sample preparation) but show a nicely preserved fine ultrastructure with e.g., visible nanopores (Figures 6-8). However, notable chemical differences are observed depending on depth in the sediments. In the first ten centimeters, the frustules are composed of silica. Morphologically well-preserved frustules become less abundant below 10 cm depth and the silica composing them gradually transforms to a poorly crystalline Mg-silicate phase, as shown by SEM- and TEM-EDXS as well as SAED (**Figures 6, 7 and 8**). Despite this chemical/mineralogical transformation, the ultrastructure sometimes remains finely preserved, showing that this mineralogical transformation is pseudomorphic. The average Mg/Si ratio of this phase as analyzed by EDXS is 0.74 ± 0.18 (n=12), which is consistent with kerolite [$Mg_3Si_4O_{10}(OH)_2.H_2O$] and stevensite [$(Ca,Na)_xMg_{3-x}(Si_4O_{10})(OH)_2.nH_2O$]. The stoichiometry estimated more finely as $Na_{0.12}K_{0.009}Ca_{0.31}Fe_{0.2}Al_{0.15}Mg_{2.65}Si_4O_{10}(OH)_2.nH_2O$ is more consistent with Al-poor stevensite (Al = 0.19±0.26 at.%, n=12). Some grains of this phase are also observed away of the diatoms and not just replacing them. In few cases, Al-containing Mg-silicates were detected but mostly in the vicinity of detrital grains in Lake Alchichica sediments

(Al = 2.41±0.85 at.%, n=20; **Figure S6**). In the literature, up to 1 wt.% of Al is commonly reported in sepiolite, kerolite and stevensite (e.g. Stoessell, 1988; Capet, 1990), sometimes reaching up to 5 wt.% (e.g. Rhouta et al. 2008 and references therein).

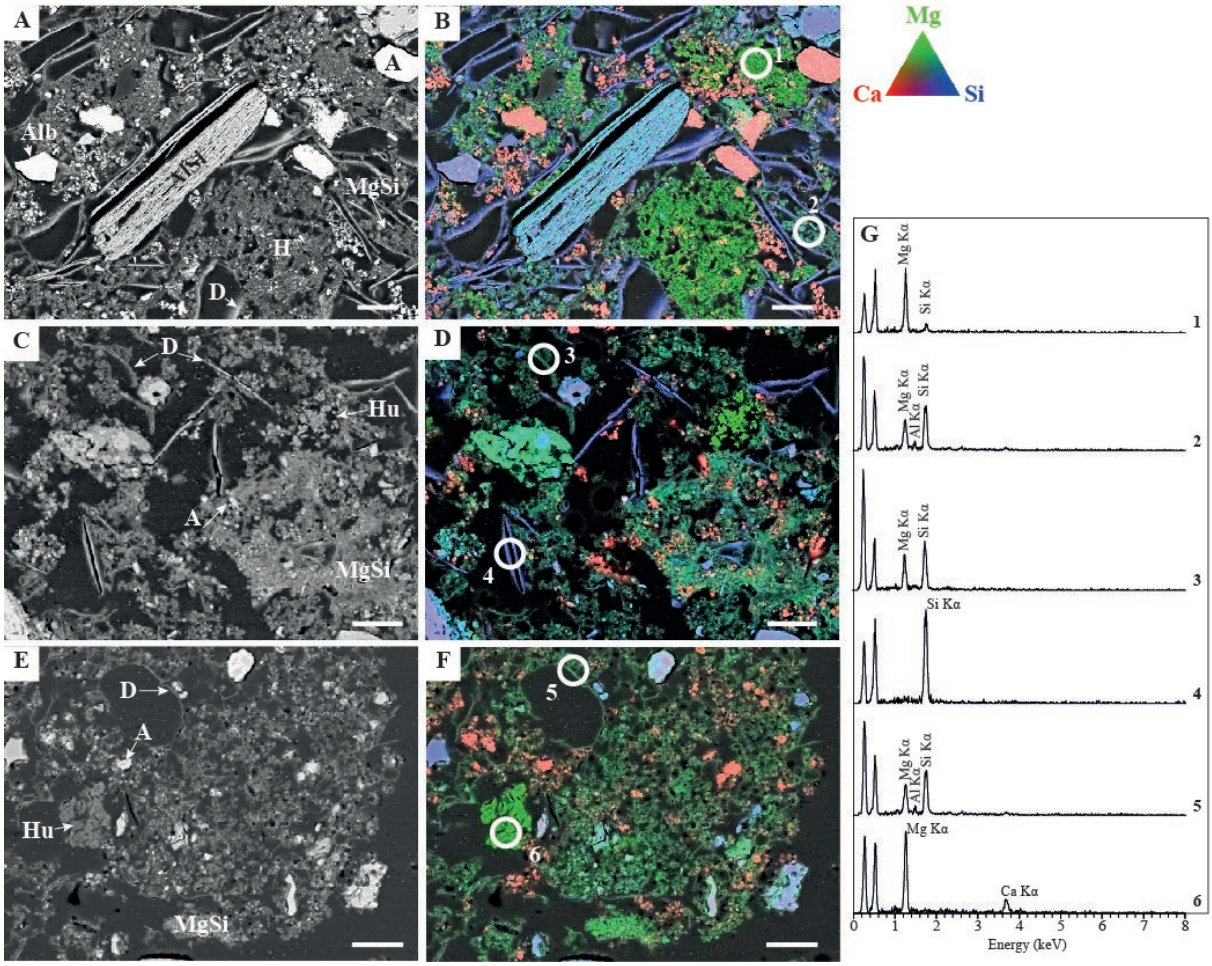

Figure 6: Evolution of the sediment mineralogy with depth. Backscattered electron (BSE) images (left) and corresponding EDXS maps (right) of Mg (green), Ca (red) and Si (blue) at 1-3 cm (A, B), 7-10 cm (C, D) and 34.5-40 cm depth in the sediment core (E, F). (G) EDXS spectra of areas circled in white. On the chemical composition maps, aragonite appears in red, silica in blue, huntite and hydromagnesite in light green and Mg-silicates in dark green. Hydromagnesite is mainly observed at 1-3 cm (spectra 1), whereas huntite is only detected at 7-10 cm and 34.5-40 cm (spectra 6). Mg-silicates with very low amount of Al (0.19±0.26 at.% in average, n=12) are detected in all the samples (spectra 2). Diatoms are progressively transformed into Mg-silicate. At 1-3 cm depth, they are mostly composed of silica, whereas at 7-10 cm depth, some are transformed into Mg-silicates (spectra 3) while others are not (spectra 4). Then, at 34.5-40 cm depth, all diatoms are replaced by Mg-silicates (spectra 5). Scale bars correspond to 20 µm. H: hydromagnesite; MgSi: Mg-silicate; D: diatom; A: aragonite; Hu: huntite; AlSi: detrital Al-silicate (containing Al, Si, Fe, K, Na, Mg).

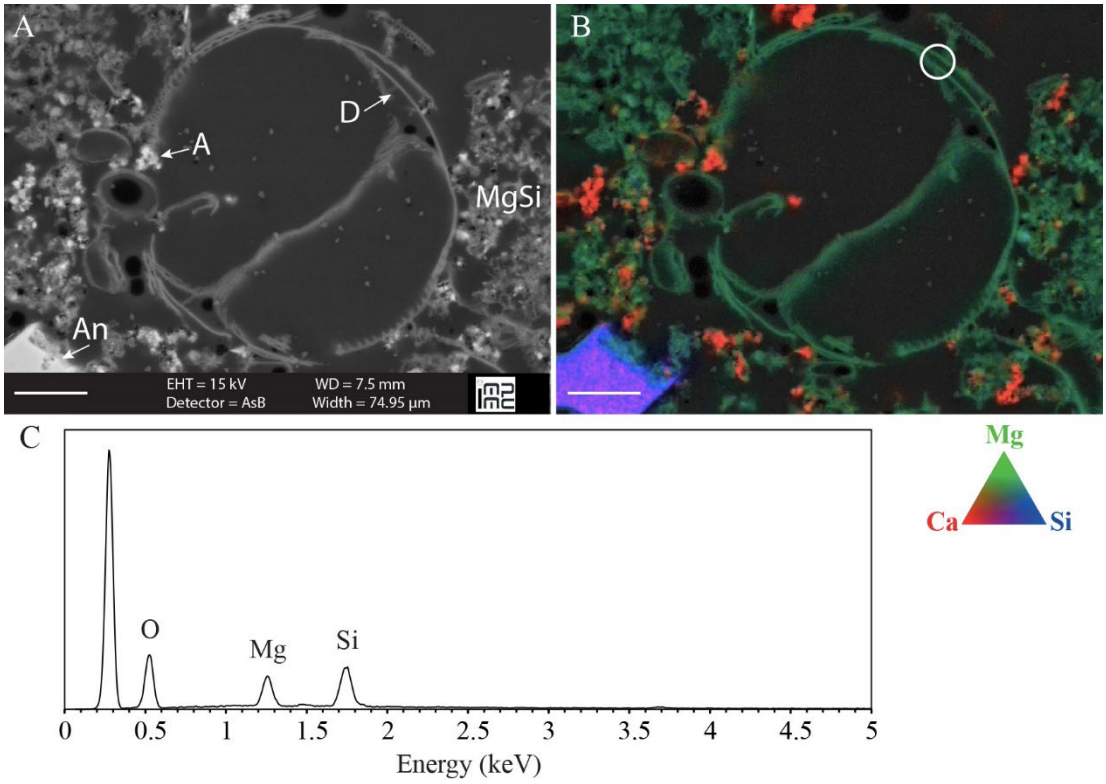

479

480 **Figure 7: Diatom composed of Mg-silicates at a 41.5 cm depth in the sediment core.** (A)
481 Backscattered electron (BSE) image, (B) corresponding EDXS map of Mg (green), Ca (red)
482 and Si (blue) and (C) EDXS spectra of the zone highlighted by a white circle. On the chemical
483 composition map, aragonite appears in red, Mg-silicates in dark green and anorthite in pink-
484 blue (at bottom left corner). Scale bars correspond to 10 µm. An: anorthite, A: aragonite, D:
485 diatom, MgSi: Mg-silicate.
486

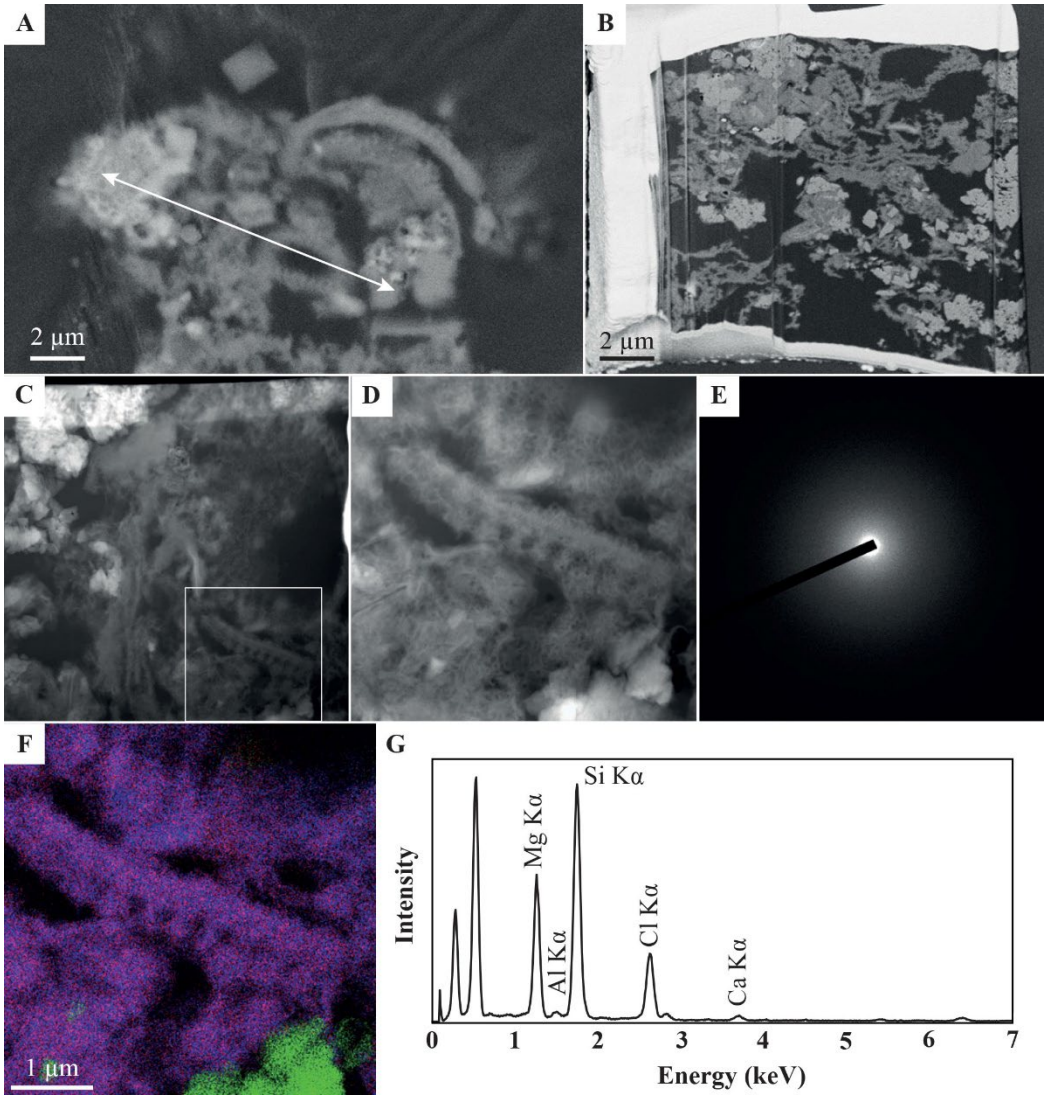

Figure 8: Scanning transmission electron microscopy (STEM) analyses of a diatom pseudomorphosed into Mg-silicates. (A) Scanning electron microscopy image showing sediment particles collected at 16-19 cm and embedded in resin. The white line indicates where the FIB section was excavated. (B) Image of the FIB foil. Aragonite appears in bright and Mg-silicates in grey. (C) STEM image in high-angle annular dark field mode (HAADF) showing sediment particles. (D) Zoom showing a diatom fragment with a fibrous texture. (E) Electron diffraction pattern measured on the diatom fragment, indicating that it is amorphous. (F) Overlay of magnesium (red), silicon (blue) and calcium (green) elemental maps as measured by energy dispersive x-ray spectrometry (EDXS). (G) EDXS spectrum obtained on the diatom fragment showing major Mg and Si peaks. Cl is attributed to resin. A small Al peak can be observed.

Bulk chemistry of the sediment solid phases

503 The bulk chemical composition of the sediments mostly consists of silicon, calcium,
504 magnesium and aluminum (**Table 2**). Titanium content shows a strong positive correlation with
505 aluminum with an y-intercept of about 0 in all sediments interpreted as a result of the shared
506 detrital origin of these two elements (**Figure 9b**). SiO_2 and Al_2O_3 also correlate positively for
507 most of the samples suggesting that Al is mostly found in silicates (**Figure 9a**). However, since
508 $[SiO_2]$ = 25.78 wt.% when $[Al_2O_3]$ = 0, phases other than detritic Al-containing silicates
509 contribute massively to the total concentration of silica in the sediments. Based on all
510 mineralogical analyses shown above, we suggest that those phases are the amorphous silica of
511 diatoms and/or authigenic Mg-silicates, depending on the depth in the core. Moreover, **Figure**
512 **9** suggests that the top sediments (from 0 to 11.5 cm) are enriched in non-detrital silica possibly
513 due to the accumulation of diatoms, whereas samples at 37.3 and 71.5 cm are depleted in non-
514 detrital silica, in agreement with FTIR and XRD data.

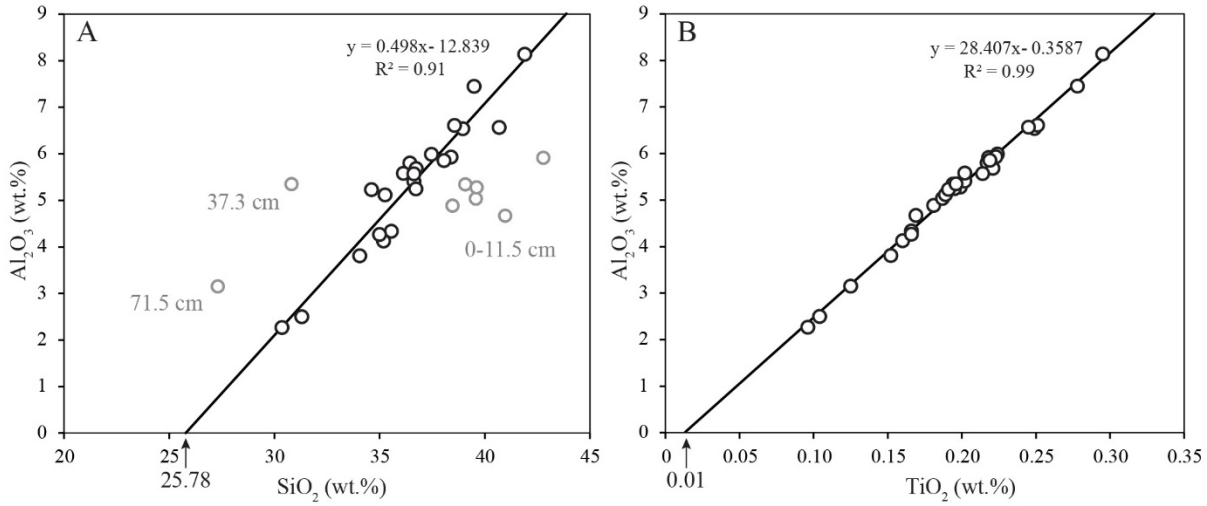

515

516 **Figure 9:** Correlation between bulk concentrations of (A) Al_2O_3 and SiO_2 and (B) Al_2O_3 and
517 TiO_2 in the sediments of Alchichica. Symbolized by grey dots, the top sediments (from 0 to
518 11.5 cm) are enriched in non-detrital silica possibly due to the accumulation of diatoms,
519 whereas samples at 37.3 and 71.5 cm are depleted in non-detrital silica, in agreement with FTIR
520 and XRD data.
521

522

523

The semi-quantitative evolution of the mineral composition with depth was assessed based on bulk chemical analyses of the sediments and relying on XRD and FTIR analyses (**Figure 10, Table S3)**. The feldspars (albite and bytownite) and aragonite contents are relatively constant along the core, between 40 and 60 wt.%. The uppermost sediments (0–3 cm) also show more than 30 wt.% of amorphous silica and 20 wt.% of hydromagnesite. Then, amorphous silica decreases with depth down to 3 wt.% in average, while Mg-silicates accumulate to reach up to 40 wt.% on average. As hydromagnesite is not detected either by XRD (**Figure S4**), FTIR (**Figure S5**) or SEM (**Figure 6**) below 3 cm in depth, it is no longer considered in the calculations. Between 30 and 40 cm in depth, sediments are devoid of silica. Concurrently, between 35 and 40 cm, they show a lower Mg-silicates content (34 wt.%) and a relatively high amount of Mg carbonates (10 wt.%. of huntite and hydromagnesite).

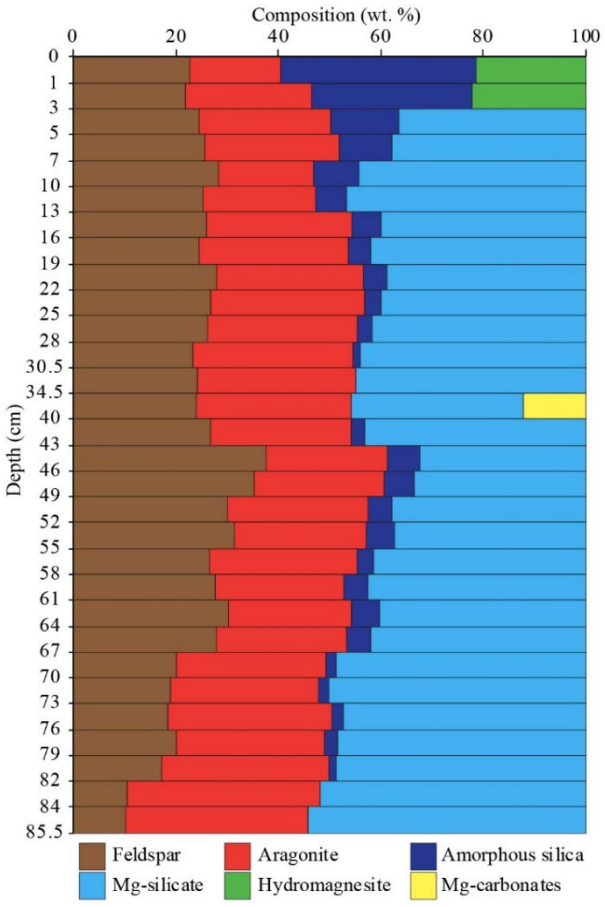

Figure 10: Estimated mineral content of the sediment (wt. %) as function of depth based on bulk chemical analyses. Minerals stoichiometry used for the quantification of mineral phases is given in Table S3.

E) Discussion

a) Massive formation of Mg-silicates in the sediments of Lake Alchichica

The uppermost sediments (0-3 cm) are dominated by hydromagnesite, aragonite, diatom frustules which settled down the water column, detrital alkaline feldspars and quartz inherited from the erosion of the surrounding volcanic rocks (**Figures 10 and 11**). The presence of aragonite and hydromagnesite in the first centimeters of sediment suggests that they precipitated in the water column or at the sediment–water interface, where solutions are oversaturated with all calcium and magnesium carbonate phases, including their potential precursors, i.e., amorphous phases (Zeyen et al., 2021). This is also consistent with the fact that these phases are found in shallow microbialites populating Lake Alchichica (Zeyen et al., 2021). However, below ~3 cm in depth, hydromagnesite rapidly disappears, and diatom frustules are progressively replaced by Al-poor Mg-silicates with a composition corresponding to stevensite, as evidenced by SEM-EDXS and STEM (**Figures 6-8**). These Mg-silicates then rapidly become a dominant phase detected by XRD, FTIR and SEM-EDXS (**Figures 4-6**), and represent between 30 and 53 wt.% of the sediment content at all depths below ~3 cm as calculated from the bulk chemistry and relying on FTIR and XRD results (**Figure 10**). Thereafter, we explain how this massive amount of Mg-silicates results from a diagenetic process occurring within the sediments and not past variations of the nature of the mineral phases settling down in the water column.

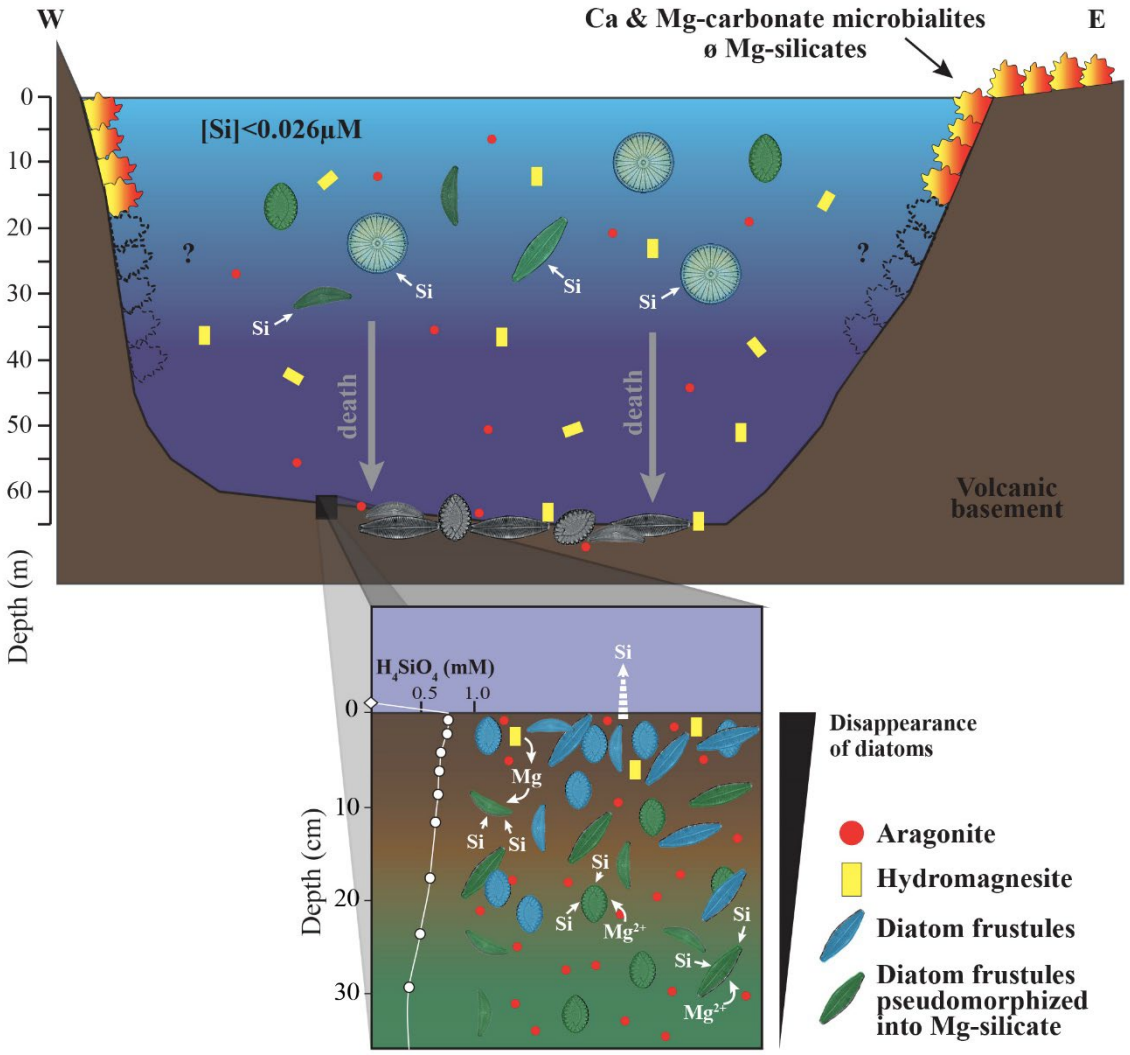

562

563 **Figure 11: Summarizing sketch of the mineralogical evolution of the first centimeters of**
564 **sediments in Lake Alchichica compared to that of the shallow microbialites populating**
565 **lake waters.** In Lake Alchichica, microbialites form at low concentrations of H_4SiO_4 in the lake
566 because the living diatoms are an active SiO_2 sink. They are mainly composed of aragonite (in
567 red) and hydromagnesite (in yellow). In contrast, in the sediments, hydromagnesite rapidly
568 disappears and diatom frustules (in blue) are progressively pseudomorphized by Al-poor Mg-
569 silicates, which become a dominant phase (in green). Therefore, the authigenesis of Mg-
570 silicates in the sediments is mainly controlled by the spontaneous dissolution of diatom frustules
571 which reduces the diffusion rate of H_4SiO_4 from the sediments to the water column.
572

573 Large amounts of authigenic Mg-silicates in modern environments are rarely described in
574 the literature. Badaut and Risacher (1983) and more recently Bentz and Peterson (2020)
575 reported authigenesis of Mg-silicates from diatom frustules (from 25 to 100% of the total
576 diatom content) in the sediments of Bolivian salars. High amounts of Mg-silicates (~296 µmol
577 Si g^{-1} sediments) were also described in the Amazon delta sediments (Michalopoulos and Aller,

1995, 2004) and in Lake Dziani Dzaha (Mayotte), including Al-poor Mg-silicate associated with shallow microbialites and up to 20 wt.% of Mg-saponite in the sediments (Gérard et al., 2018; Milesi et al., 2019, 2020). Interestingly, the high proportion of Mg-silicates in Lake Alchichica sediments contrasts with the absence of authigenic Mg-silicates in Alchichica shallow microbialites (Zeyen et al., 2019). Zeyen et al. (2021) systematically assessed the presence/absence of authigenic Mg-silicates in microbialites from 10 Mexican alkaline crater lakes. They showed that microbialites from most lakes contained Mg-silicates except those in Lake Alchichica. The authors suggested that this difference may result from the very low orthosilicic acid concentration in Lake Alchichica (64 ± 94 µM) compared with other lakes (e.g., 1.10 and 0.58 mM in Lakes Atexcac and La Preciosa, respectively; Zeyen et al., 2021), and therefore that water was not saturated enough to allow spontaneous precipitation. They also speculated about the potential causes for a lower acid orthosilicic acid concentration in the water column of Lake Alchichica, mentioning variations in the nature of the weathered protolith and the active extraction of orthosilicic acid by diatoms, similar to what has been shown in oceans (Conley et al., 2017). As explained thereafter, the formation of Mg-silicates in Lake Alchichica sediments results from a diagenetic process which locally increases the orthosilicic acid concentrations highly enough to allow the precipitation of these phases. The source of the orthosilicic acid is discussed in the next section.

b) Geochemical processes involved in the formation of Mg-silicates

Here, we discuss the processes that may explain the evolution at depth of the mineralogical composition of Lake Alchichica sediments, i.e., the correlated disappearance of Mg-carbonates and amorphous silica and appearance of Mg-silicates. In the sediments of Lake Alchichica, the

602 formation of Mg-silicates may result from three different mechanisms providing alternate Mg
603 and/or Si sources:
604 (1) a reaction between detrital silicates as the main source of Si and hydromagnesite as the
605 source of Mg, along the same mechanism as that mentioned by Milesi et al. (2018) for the
606 sediments of Lake Dziani Dzaha (Mayotte), and following the equation:
607 $1.8Mg_5(OH)_2(CO_3)_4{\cdot}4H_2O + 4KAlSi_3O_8 + 8.8H^+ \Rightarrow 3Mg_3Si_4O_{10}(OH)_2{\cdot}H_2O + 4Al^{3+} + 4K^+ +$
608 $7.2HCO_3^- + 3.8H_2O$
609 (2) a reaction between diatom frustules as the main source of Si and hydromagnesite as the
610 source of Mg:
611 $3Mg_5(CO_3)_4(OH)_2{\cdot}4H_2O + 20SiO_2 + 7H_2O \Rightarrow 5Mg_3Si_4O_{10}(OH)_2{\cdot}H_2O + 12HCO_3^- + 12H^+$
612 (3) the same reaction as in (2) with aqueous Mg^{2+} from porewater instead of hydromagnesite:
613 $3Mg^{2+} + 4SiO_2 + 5H_2O \Rightarrow Mg_3Si_4O_{10}(OH)_2{\cdot}H_2O + 6H^+$
614
615 Detrital silicates, which represent 12 to 39 wt.% of the sediment content, could be a
616 source of silica for the formation of Mg-silicates similarly as in Lake Dziani Dzaha. In Dziani
617 Dzaha, the diagenetic Mg-silicates contain significant amounts of Al (3.65 wt.% in average;
618 Milesi et al., 2018). Accordingly, we observed some Al-containing Mg-silicates. However, they
619 were rare and mostly spatially associated with altered detrital silicate phases (**Figures 6 and**
620 **S6**). By contrast, diatom frustules appear as a more likely source of SiO_2 involved in the
621 diagenetic formation of Mg-silicates in Lake Alchichica sediments. First, they are abundant
622 enough (around 35 wt.% of the uppermost sediments) to provide all Si necessary for the
623 formation of the Mg-silicates detected in the sediments. Second, there is very good correlation
624 between the disappearance of the FTIR bands of amorphous silica and the concomitant
625 appearance of silicates bands below 10 cm (**Figure 5**). Last, we observed by SEM and TEM a
626 massive pseudomorphic replacement of the amorphous silica composing diatoms by Mg-

627 silicates, providing direct images of this diagenetic process (**Figures 7-8**). It can be noted that
628 some Mg-silicate grains do not form as pseudomorphic replacements of diatoms but likely
629 precipitate in the porewater containing high orthosilicic acid concentrations dissolved from
630 diatoms. Authigenesis of Mg-silicates on diatom frustules was previously observed in the
631 sediments of Bolivian saline lakes (Badaut, 1979; Hoffert, 1980; Badaut and Risacher, 1983;
632 Bentz and Peterson, 2020) and marine settings (Michalopoulos and Aller, 2004). The
633 pseudomorphic replacement of the amorphous silica of diatoms by Mg-silicates was also
634 occasionally observed in some microbialites (e.g., Zeyen et al. 2021) but this did not produce
635 the massive amounts of Mg-silicates as observed in Lake Alchichica sediments.
636
637 In the case of a replacement of diatoms by Mg-silicates, two sources of Mg can
638 contribute to this process: hydromagnesite and/or dissolved Mg^{2+}. In Lake Alchichica
639 sediments, hydromagnesite disappears below the first 3 cm of sediments, possibly entirely
640 consumed by reaction (2). Using chemical and mineralogical data, we calculated that the 20
641 wt.% of hydromagnesite present in the uppermost sediments (at 0-3 cm depth) represent 0.17
642 mmol of Mg /g sediment. However, 42 wt.% of Mg-silicates are formed along the core, which
643 represent 0.24 mmol of Mg /g sediment on average (at 41-85 cm; n=16). Therefore, some
644 dissolved Mg^{2+} may also contribute to the formation of Mg-silicates by reaction (3). In addition,
645 between 30 and 40 cm depth, hydromagnesite is not totally consumed. Therefore, we suggest
646 that a lower input of diatoms to the sediments from this depth, at the time they settled down,
647 limited the reaction of Mg-silicates formation, preserving some hydromagnesite. Overall, this
648 suggests that the amount of amorphous silica provided by the diatom frustules (and therefore
649 the ecological dynamics of diatom populations in the lake) is one major control of the extent of
650 Mg-silicates authigenesis in Lake Alchichica sediments.
651

c) Geochemical conditions necessary for the authigenesis of Mg-silicates in sediments

While the replacement of amorphous silica by Mg-silicates is massive in Lake Alchichica sediments and possibly other lakes, it does not obviously occur in all lakes. Here we discuss the conditions necessary for this process to take place. In this purpose, the chemical composition of the porewater is helpful. Pore waters in the first 10 centimeters of the sediments had a constant orthosilicic acid activity (**Figure 3**), around 661±24 on average, suggesting a potential control by the solubility of a silica phase that would have a log(Ks) of -3.18 (log(Ks)=log(a[H_4SiO_4]); Figure S7). This value is consistent with what is known for the solubility of diatom silica. Indeed, the solubility constant of diatom frustules is known to be variable and a function of the physicochemical properties of the solid material (e.g. degree of condensation and order of the silica framework, water and impurity contents, specific surface area; Willey, 1980; Hurd and Birdwhistell, 1983; Beck et al., 2002; Dixit and Van Cappellen, 2002; Gehlen and Van Raaphorst, 2002; Loucaides et al., 2012a,) and of the surrounding solution (e.g., temperature, salinity, pressure; Loucaides et al., 2012b). As a result, it likely varies substantially between different diatom species. Overall, it has been shown that diatomaceous silica solubilities exhibit a large variability from 200 to 1600 µM in seawater (log(Ks) between -3.70 and -2.79; Loucaides et al., 2012a, 2012b and references therein). Badaut and Risacher (1983) observed similar solubilities in continental saline lakes around -3. Therefore, the log(Ks) of -3.18 tentatively inferred from the chemical measurements in the porewater of Lake Alchichica is consistent with an equilibrium of porewaters with the amorphous silica phase composing the abundant diatoms of the sediments.

Below 11.5 cm in depth in the sediments, the activity of orthosilicic acid is no longer constant, which is consistent with the observed disappearance of silica in the solid by, e.g., FTIR. However, the $\log[a(Mg^{2+})/a(H^{+})^2]$ / $\log[a(H_4SiO_4)]$ becomes constant (see trend 2 in **Figure 3**), i.e., in a $\log[a(Mg^{2+})/a(H^{+})^2]$ vs $\log[a(H_4SiO_4)]$ graph, porewaters become aligned along a trend parallel to the solubility line of the "amorphous sepiolite" defined by Wollast et al. (1968) at 25°C (with a log(Ks) of 18.78). The log(Ks) inferred for the Mg-silicate phase observed in Alchichica sediments at 15°C is 19.26 (Figure S7). This strongly suggests that below 11.5 cm depth, a Mg-silicate phase with this solubility controls the activities of protons, Mg^{2+} and orthosilicic acids in the porewater. This is again in agreement with the fact that such a phase becomes a dominant Si and Mg-bearing phase in the sediments at these depths. This also answers the question of the geochemical conditions necessary for the formation of Mg-silicates in sediments: the ionic product of the solution should be higher or equal to the solubility of a Mg-silicate phase close to that of "amorphous sepiolite".

Tosca et al. (2011) suggested that a much higher saturation of the solution was needed so that precipitation could spontaneously occur. According to them, the different solubility constants obtained by their study *vs*. that by Wollast et al. (1968) were related to the source of Si used in their experiments (i.e., respectively sodium metasilicate nonahydrate *versus* tetraethyl orthosilicate). Here, the observations point to a phase less soluble than that formed in Tosca et al. (2011)'s experiments. However, the critical supersaturation line defined by these authors refers to the conditions allowing homogeneous nucleation of Mg-silicates. In Alchichica sediments, the replacement of the diatom frustules by Mg-silicates likely involves heterogeneous nucleation, which is known to occur at lower saturations than homogenous nucleation. Therefore, this may explain why the solubility of the Mg-silicate phase formed in the sediments of Lake Alchichica is lower than the one determined by Tosca et al. (2011) and

701 closer to that of the "amorphous sepiolite" defined by Wollast et al. (1968). In any case, we
702 suggest that the solubility constant determined here should be considered when modelling the
703 formation of Mg-silicates in a natural environment.
704
705 Now that the geochemical conditions necessary for the formation of Mg-silicates are better
706 assessed, we can understand some other observations. First, despite oversaturation relative to
707 the reported solubilities of Mg-silicate phases such as kerolite, stevensite, talc and sepiolite
708 below 30 m depth, the whole water column of Lake Alchichica remains undersaturated with
709 "amorphous sepiolite". This explains why no Mg-silicate was observed in the mineral
710 assemblage of the uppermost sediments, suggesting that they do not precipitate from the lake
711 water. Second, porewaters in Lake Dziani Dzaha sediments were undersaturated with
712 "amorphous sepiolite" at almost all depths, explaining why Al-poor Mg-silicates could not form
713 there and therefore were not observed (**Figure S7**). One reason why the saturation in Lake
714 Dziani sediments might be lower than in Lake Alchichica and Bolivian saline lakes sediments
715 (Badaut and Risacher, 1983) may relate to the low abundance of diatoms in the water column
716 of this lake (Gérard et al., 2018). However, Mg-silicates detected in the sediments of Lake
717 Dziani Dzaha were rich in Al (Milesi et al., 2019) in contrast to those observed in Alchichica
718 sediments. Al-rich Mg-silicates have a lower solubility (Milesi et al., 2020), explaining why
719 those phases may form in Lake Dziani Dzaha sediments.
720 In Lake Dziani Dzaha, the formation of Mg-silicates from detrital silicates by reaction (1)
721 consumes protons and can therefore be driven by a pH decrease. Milesi et al. (2019, 2020)
722 proposed that oxidation of organic matter and input of volcanic CO_2 tend to decrease the pH of
723 porewaters, which promotes destabilization of hydromagnesite and ultimately allows Mg
724 supply for the formation of saponite. In Lake Alchichica sediments, the decrease of pH from
725 9.25 to 8.46 and the DIC increase from 34.1 to 43.2 mM may as well reflect oxidation of organic

matter and/or input of volcanic CO_2. However, reactions (2) and (3) based on diatom transformation produce protons instead of consuming them. Therefore, these reactions are favored by a pH increase, provided that concentrations of Mg and Si are high enough to reach the supersaturation with respect to Mg-silicates precursors, i.e. "amorphous sepiolite". We thus suggest that in Alchichica sediments, the spontaneous dissolution of the diatom frustules and not organic matter mineralization drives Mg-silicates authigenesis.

d) Some implications of massive authigenesis of Mg-silicates

We can note three possible geochemical implications associated with the massive authigenesis of Mg-silicates in Lake Alchichica sediments.

First, the precipitation of Mg-silicates in Alchichica sediments imposes lower dissolved H_4SiO_4 concentrations in porewaters than if they were in equilibrium with the silica of diatoms (such as in the top 10 cm of sediment, **Figure 3**). Therefore, we suggest that H_4SiO_4 concentration gradient between the sediments and the water column is also lower, decreasing the diffusion rate of this species from the sediments to the water column. Accordingly, although the H_4SiO_4 concentration increases with lake water depth from below the detection limit to 0.026 mM at 60 m depth and 0.084 mM at the sediment interface, it is much lower than the pore water concentration of 0.76 mM (**Table 1**). This low Si release rate from the sediments, in addition to a possibly higher abundance of diatoms in the water column, could ultimately favor the low concentrations of H_4SiO_4 observed in Lake Alchichica compared with other lakes around (namely Lakes Atexcac and La Preciosa).

Second, the diagenetic formation of Mg-silicates calls for care when interpreting the paleoenvironmental message carried by the sedimentary record. The presence/absence of Mg-silicates has been suggested to provide information about the paleochemistry of lakes. However,

751 in Lake Alchichica, we observed on the one hand shallow microbialitic deposits without Mg-
752 silicate and on the other hand deep sediments dominated by Mg-silicates. A basin-wide
753 assessment should therefore be considered whenever possible. In the modern system of Lake
754 Alchichica, it is clear that stromatolites form at low concentrations of H_4SiO_4 in the lake
755 because the living diatoms are an active SiO_2 sink, whereas in the sediments, the dead diatoms
756 are a source of Si that feeds the Mg-silicates precipitation. How likely can we find signatures
757 of this process in ancient sediments? Although fossilization of microorganisms by silicates was
758 occasionally observed in modern microbialites (Zeyen et al., 2015), the preservation of diatom
759 morphologies/structures in sediments is not systematic (Michalopoulos and Aller, 2004). In
760 Alchichica, they rather gradually disappear through the massive authigenesis of Mg-silicate
761 around diatoms **(Figure 6**). Therefore, the presence/absence of diatoms is not a robust criterion
762 to identify this diagenetic process in the past.

763 Last, better understanding silicate authigenesis in a variety of environments is key to
764 evaluate the effect of reverse weathering and especially its involvement in the long-term cycles
765 of C and Si (Mackenzie and Kump, 1995). Reverse weathering refers to the reactions that
766 produce authigenic silicates, which consumes soluble cations generated by silicate weathering,
767 but unlike carbonates do not consume carbon (e.g., Isson and Planavsky, 2018; Krissansen-
768 Totton and Catling, 2020). Therefore, it affects not only Si and C cycles but also the climate by
769 retaining CO_2 within the atmosphere-ocean system. While robust evidence for clay authigenesis
770 in modern environments has emerged (Badaut and Risacher, 1968; Michalopoulos and Aller,
771 1995; Wallmann et al., 2008; Ehler et al., 2016; Bentz and Peterson, 2020), both laboratory
772 studies (Michalopoulos and Aller, 1995) and analyses of natural marine sediments (Wallmann
773 et al., 2008; Ehler et al., 2016) suggest that it is almost exclusively restricted to environments
774 characterized by extremely high rates of biogenic opal remineralization (Michalopoulos and
775 Aller, 2004; Ehler et al., 2016). This type of environments is supposedly rare. Consequently,

776 reverse weathering is generally estimated to constitute only a relatively minor (<10%)
777 component of total dissolved silica export in the modern oceans (e.g. Wallmann et al., 2008).
778 Here, we show a continental system in which Mg-silicate authigenesis by diatom
779 remineralization is major. This allowed us to refine the conditions under which authigenesis
780 occurs. Furthermore, models have tried to quantify reverse weathering over geological times
781 (Isson and Planavsky, 2018; Krissansen-Totton and Catling, 2020). In the Precambrian, before
782 the advent of significant biogenic silica precipitation, ocean silica concentrations were likely
783 elevated (Siever, 1992; Conley et al., 2017), deriving from continental and seafloor weathering
784 (Isson and Planavsky, 2018). Isson and Planavsky (2018) argued that these elevated silica levels
785 may have increased the reverse weathering flux, maintained high levels of CO_2, and warmed
786 the Precambrian climate. Additionally, these authors proposed that reverse weathering is
787 strongly pH dependent, and thus may have buffered ocean pH and stabilized the atmosphere-
788 ocean pCO_2 during the Precambrian. A key parameter in these models is the solubility of
789 authigenic silicates, which has been determined by laboratory experiments and is still debated
790 (Wollast et al., 1968; Tosca et al., 2011). Here, we provide a solubility constant deduced from
791 a natural system, lower than the one proposed by Tosca et al. (2011) and Tosca and Masterson
792 (2014). Therefore, despite there is no observational evidence to date suggesting a greater
793 importance of reverse weathering in the past, its proportion associated with this solubility
794 constant could be higher than predicted by Tosca et al. (2011) and thus have a greater impact
795 on pH buffering potential of the oceans and climate regulation. We also showed that Mg-silicate
796 authigenesis in Alchichica is strongly driven by diatoms, which appeared late in geological
797 history, likely during the Cretaceous (Girard et al., 2020). Earlier organisms such as sponges,
798 radiolarians and some bacteria (Li et al., 2022) may have produced silica-rich sediments by
799 biomineralization as well in the past, which may have fed this reverse weathering process in
800 the same way.

F) Conclusion

Alchichica lacustrine sediments exhibit a particular mineralogical evolution in their first centimeters, which can be explained by early diagenetic reactions (**Figure 11**). Below ~3 cm in depth, hydromagnesite rapidly disappears and diatom frustules are progressively pseudomorphized by an Al-poor Mg-silicate phase with a composition corresponding to stevensite. Interestingly, the replacement of amorphous silica by Mg-silicates is massive in Lake Alchichica sediments and contrasts with the absence of authigenic Mg-silicates in Alchichica shallow microbialites, mainly composed of aragonite and hydromagnesite (**Figure 11**). This observation raises questions about the paleoenvironmental message carried by the sedimentary record, since the presence/absence of Mg-silicates is considered to provide information about the paleochemistry of lakes. However, in Lake Alchichica, microbialites form at low concentrations of H_4SiO_4 in the lake because the living diatoms are an active SiO_2 sink, whereas in the sediments, the spontaneous dissolution of the diatom frustules drives the Mg-silicates precipitation (**Figure 11**). Therefore, an appraisal at the basin scale should be considered whenever possible. Moreover, this study confirms that the preservation of diatom morphologies/structures in sediments is not systematic, and not a robust criterion to identify this process in the past.

In Lake Alchichica sediments, Mg-silicate authigenesis by diatom pseudomorphosis occurs in porewaters saturated with "amorphous sepiolite" as defined by Wollast et al. (1968) (**Figure 3**). The solubility constant deduced from this study (log(Ks) = 19.26 at 15°C) is thus lower than the one proposed by Tosca et al. (2011) and Tosca and Masterson (2014) (log(Ks) = 33.82 at 25°C). We propose that it should be considered when modelling the formation of Mg-silicates

in a natural environment. The reassessment of this higher solubility constant suggests that reverse weathering may have a greater impact on climate stabilization than previously thought.

Acknowledgement

This work was supported by IMPMC (Muséum National d'Histoire Naturelle de Paris and Sorbonne University, France), and Agence Nationale de la Recherche (France; ANR Microbialites, grant number ANR-18-CE02-0013-02). We thank Ludovic Delbes and Benoit Baptiste who managed the XRD platform at IMPMC where analyses were performed. We thank Keevin Beneut and Maxime Guillaumet who managed the FTIR platform at IMPMC where analyses were performed. We thank Imene Esteve, Béatrice Doisneau and Stéphanie Delbrel who managed the SEM platform at IMPMC where analyses were performed. We thank Laure Cordier for performing ion chromatography analyses at IPGP (France) and Céline Liorzou for performing ICP-AES analyses at Pôle Spectrométrie Océan (Laboratoire Géo-Océan, Brest, France). The authors declare no conflict of interest.

Data Availability Statement

The data that supports the findings of this study are included in this article and available in supplementary material.

References

Alcocer, J., & Hammer, U. T. (1998). Saline lake ecosystems of Mexico. *Aquatic Ecosystem Health & Management*, 1(3-4), 291-315.

Alcocer, J., Lugo, A., Escobar, E., Sánchez, M. D. R., & Vilaclara, G. (2000). Water column stratification and its implications in the tropical warm monomictic Lake Alchichica, Puebla, Mexico. *Internationale Vereinigung für theoretische und angewandte Limnologie: Verhandlungen*, 27(5), 3166-3169.

Alcocer, J., & Oseguera, L. A. (2019). Lago Alchichica: Una joya de biodiversidad. In: *El cuerpo de agua.* Ed. Facultad de Estudios Superiores Iztacala, Universidad Nacional Autónoma de México. Comisión Nacional para el Conocimiento y Uso de la Biodiversidad. Mexico City, 1a edición. pp. 63-75.

Alcocer, J. (2021). *Lake Alchichica limnology. The Uniqueness of a Tropical Maar Lake*. Springer Nature: Berlin/Heidelberg, Germany, 491.

Armienta, M. A., Vilaclara, G., De la Cruz-Reyna, S., Ramos, S., Ceniceros, N., Cruz, O., Aguayo, A., & Arcega-Cabrera, F. (2008). Water chemistry of lakes related to active and inactive Mexican volcanoes. *Journal of Volcanology and Geothermal Research*, 178(2), 249-258.

Arp, G., Reimer, A., & Reitner, J. (2003). Microbialite formation in seawater of increased alkalinity, Satonda Crater Lake, Indonesia. *Journal of sedimentary research*, 73(1), 105-127.

Arredondo-Figueroa, J. L., Borrego-Enríquez, L. E., Castillo-Domínguez, R. M., & Valladolid-Laredo, M. A. (1983). Batimetría y morfometría de los lagos "maars" de la cuenca de Oriental, Puebla, México. *Biótica*, 8(1), 37-47.

Arredondo-Figueroa, J. L. (2002). Los axalapascos de la cuenca oriental, Puebla. In : *Lagos y presas de México.* (Ed. G. De la Lanza E. y JL García C), compiladores, AGT. México, DF, pp. 81-107.

869 **Assayag, N.,** Rivé, K., Ader, M., Jézéquel, D., & Agrinier, P. (2006). Improved method for
870 isotopic and quantitative analysis of dissolved inorganic carbon in natural water samples.
871 *Rapid Communications in Mass Spectrometry*, 20(15), 2243-2251.
872 **Badaut, D.,** Risacher, F., Paquet, H., Eberhart, J. P., & Weber, F. (1979). Néoformation de
873 minéraux argileux à partir de frustules de diatomées : le cas des lacs de l'Altiplano bolivien.
874 *Comptes Rendus de l'Académie des Sciences*, 1191-1193.
875 **Badaut, D., & Risacher, F.** (1983). Authigenic smectite on diatom frustules in Bolivian saline
876 lakes. *Geochimica et Cosmochimica Acta*, 47(3), 363-375.
877 **Beck, L.,** Gehlen, M., Flank, A. M., Van Bennekom, A. J., & Van Beusekom, J. E. E. (2002).
878 The relationship between Al and Si in biogenic silica as determined by PIXE and XAS.
879 *Nuclear Instruments and Methods in Physics Research Section B: Beam Interactions with*
880 *Materials and Atoms*, 189(1-4), 180-184.
881 **Benzerara, K.,** Menguy, N., Guyot, F., Vanni, C., & Gillet, P. (2005). TEM study of a silicate-
882 carbonate-microbe interface prepared by focused ion beam milling. *Geochimica et*
883 *Cosmochimica Acta*, 69(6), 1413-1422.
884 **Benzerara, K.,** Meibom, A., Gautier, Q., Kaźmierczak, J., Stolarski, J., Menguy, N., & Brown,
885 G. E. (2010). Nanotextures of aragonite in stromatolites from the quasi-marine Satonda
886 crater lake, Indonesia. *Geological Society, London, Special Publications*, 336(1), 211-224.
887 **Blanc, P.,** Lassin, A., Piantone, P., Azaroual, M., Jacquemet, N., Fabbri, A., & Gaucher, E. C.
888 (2012). Thermoddem: A geochemical database focused on low temperature water/rock
889 interactions and waste materials. *Applied geochemistry*, 27(10), 2107-2116.
890 **Bontognali, T. R.,** Vasconcelos, C., Warthmann, R. J., Bernasconi, S. M., Dupraz, C.,
891 Strohmenger, C. J., & McKENZIE, J. A. (2010). Dolomite formation within microbial mats
892 in the coastal sabkha of Abu Dhabi (United Arab Emirates). *Sedimentology*, 57(3), 824-844.
893 **Bristow, T. F.,** Kennedy, M. J., Derkowski, A., Droser, M. L., Jiang, G., & Creaser, R. A.
894 (2009). Mineralogical constraints on the paleoenvironments of the Ediacaran Doushantuo
895 Formation. *Proceedings of the National Academy of Sciences*, 106(32), 13190-13195.
896 **Bristow, T. F., & Milliken, R. E.** (2011). Terrestrial perspective on authigenic clay mineral
897 production in ancient martian lakes. *Clays and Clay Minerals*, 59(4), 339-358.
898 **Burne, R. V.,** Moore, L. S., Christy, A. G., Troitzsch, U., King, P. L., Carnerup, A. M., &
899 Hamilton, P. J. (2014). Stevensite in the modern thrombolites of Lake Clifton, Western
900 Australia: A missing link in microbialite mineralization? *Geology*, 42(7), 575-578.
901 **Chahi, A.,** Fritz, B., DuPlay, J., Weber, F., & Lucas, J. (1997). Textural transition and genetic
902 relationship between precursor stevensite and sepiolite in lacustrine sediments (Jbel
903 Rhassoul, Morocco). *Clays and Clay Minerals*, 45(3), 378-389.
904 **Conley, D. J.,** Frings, P. J., Fontorbe, G., Clymans, W., Stadmark, J., Hendry, K. R., Marron,
905 A. O., & De La Rocha, C. L. (2017). Biosilicification drives a decline of dissolved Si in the
906 oceans through geologic time. *Frontiers in Marine Science*, 4, 397.
907 **Couradeau, E.,** Benzerara, K., Moreira, D., Gerard, E., Kaźmierczak, J., Tavera, R., & López-
908 García, P. (2011). Prokaryotic and eukaryotic community structure in field and cultured
909 microbialites from the alkaline Lake Alchichica (Mexico). *PloS one*, 6(12), e28767.
910 **Couradeau, E.,** Benzerara, K., Gérard, E., Estève, I., Moreira, D., Tavera, R., & López-García,
911 P. (2013). Cyanobacterial calcification in modern microbialites at the submicrometer scale.
912 *Biogeosciences*, 10(8), 5255-5266.
913 **Cuadros, J.,** Diaz-Hernandez, J. L., Sanchez-Navas, A., Garcia-Casco, A., & Yepes, J. (2016).
914 Chemical and textural controls on the formation of sepiolite, palygorskite and dolomite in
915 volcanic soils. *Geoderma*, 271, 99-114.
916 **d'Espinose de la Caillerie, J. B.,** Kermarec, M., & Clause, O. (1995). ^{29}Si NMR observation
917 of an amorphous magnesium silicate formed during impregnation of silica with Mg(II) in
918 aqueous solution. *The Journal of Physical Chemistry*, 99(47), 17273-17281.

Deocampo, D. M. (2005). Evaporative evolution of surface waters and the role of aqueous CO_2 in magnesium silicate precipitation: Lake Eyasi and Ngorongoro Crater, northern Tanzania. *South African Journal of Geology*, 108(4), 493-504.

Deocampo, D. M. (2015). Authigenic clay minerals in lacustrine mudstones. *Geological Society of America Special Papers*, 515, SPE515-03.

Dixit, S., & Van Cappellen, P. (2002). Surface chemistry and reactivity of biogenic silica. *Geochimica et Cosmochimica Acta*, 66(14), 2559-2568.

Ehlert, C., Doering, K., Wallmann, K., Scholz, F., Sommer, S., Grasse, P., Geilert, S., & Frank, M. (2016). Stable silicon isotope signatures of marine pore waters–Biogenic opal dissolution versus authigenic clay mineral formation. *Geochimica et Cosmochimica Acta*, 191, 102-117.

Farmer, V. C. (1974). *The infrared spectra of minerals*. (Ed. Mineralogical Society: London).

Ferrari, L., Orozco-Esquivel, T., Manea, V., & Manea, M. (2012). The dynamic history of the Trans-Mexican Volcanic Belt and the Mexico subduction zone. *Tectonophysics*, 522, 122-149.

Fukushi, K., & Matsumiya, H. (2018). Control of water chemistry in alkaline lakes: solubility of monohydrocalcite and amorphous magnesium carbonate in $CaCl_2$–$MgCl_2$–Na_2CO_3 solutions. *ACS Earth and Space Chemistry*, 2(7), 735-744.

Galán, E., & Pozo, M. (2011). Palygorskite and sepiolite deposits in continental environments. Description, genetic patterns and sedimentary settings. In: *Developments in clay science* (Vol. 3, pp. 125-173). Elsevier.

García Martínez, J. (2010). Efectos climáticos sobre el agua subterránea y el Lago Alchichica, Puebla, México (Doctoral dissertation, Dissertation, Universidad Nacional Autónoma de México).

Gehlen, M., & Van Raaphorst, W. (2002). The role of adsorption–desorption surface reactions in controlling interstitial $Si(OH)_4$ concentrations and enhancing $Si(OH)_4$ turn-over in shallow shelf seas. *Continental Shelf Research*, 22(10), 1529-1547.

Gérard, E., Ménez, B., Couradeau, E., Moreira, D., Benzerara, K., Tavera, R., & López-García, P. (2013). Specific carbonate–microbe interactions in the modern microbialites of Lake Alchichica (Mexico). *The ISME journal*, 7(10), 1997-2009.

Gérard, E., De Goeyse, S., Hugoni, M., Agogué, H., Richard, L., Milesi, V., Guyot, F., Lecourt, L., Borensztajn, S., Joseph, M.-B., Leclerc, T., Sarazin, G., Jézéquel, D., Leboulanger, C., & Ader, M. (2018). Key role of alphaproteobacteria and cyanobacteria in the formation of stromatolites of Lake Dziani Dzaha (Mayotte, Western Indian Ocean). *Frontiers in Microbiology*, 9, 796.

Girard, V., Saint Martin, S., Buffetaut, E., Saint Martin, J. P., Néraudeau, D., Peyrot, D., Roghi, G., Ragazzi, E., & Suteethorn, V. (2020). Thai amber: insights into early diatom history? BSGF-Earth Sciences Bulletin, 191, 191.

Hoffert, M. (1980). Les" Argiles rouges des grands fonds" dans le Pacifique Centre-Est. In : *Authigenese, transport, diagenese* (Vol. 61, No. 1). Persée-Portail des revues scientifiques en SHS.

Hollingbery, L. A., & Hull, T. R. (2012). The thermal decomposition of natural mixtures of huntite and hydromagnesite. *Thermochimica acta*, 528, 45-52.

Hurd, D. C., & Birdwhistell, S. (1983). On producing a more general model for biogenic silica dissolution. *American Journal of Science*, 283(1), 1-28.

Iniesto, M., Moreira, D., Reboul, G., Deschamps, P., Benzerara, K., Bertolino, P., Saghaï, A., Tavera, R., & López-García, P. (2021). Core microbial communities of lacustrine microbialites sampled along an alkalinity gradient. *Environmental Microbiology*, 23(1), 51-68.

Işik Ece, Ö. (1998). Diagenetic transformation of magnesite pebbles and cobbles to sepiolite (meerschaum) in the Miocene Eskisehir lacustrine basin, Turkey. *Clays and Clay Minerals*, 46(4), 436-445.

Isson, T. T., & Planavsky, N. J. (2018). Reverse weathering as a long-term stabilizer of marine pH and planetary climate. *Nature*, 560(7719), 471-475.

Jones, B. F., & Mumpton, F. A. (1986). Clay mineral diagenesis in lacustrine sediments. *US Geological Survey Bulletin*, 1578, 291-300.

Jones, B.F., & Galan, E. (1988). Sepiolite and palygorskite. *Rev. Mineralogy* 19, 631–674.

Kangal, O., Firat, C., & Güney, A. (2005). Flotation properties of unusual carbonates: huntite and hydromagnesite. *Minerals engineering*, 18(6), 631-634.

Kaźmierczak, J., Kempe, S., Kremer, B., López-García, P., Moreira, D., & Tavera, R. (2011). Hydrochemistry and microbialites of the alkaline crater lake Alchichica, Mexico. *Facies*, 57(4), 543-570.

Krissansen-Totton, J., & Catling, D. C. (2020). A coupled carbon-silicon cycle model over Earth history: Reverse weathering as a possible explanation of a warm mid-Proterozoic climate. *Earth and Planetary Science Letters*, 537, 116181.

Léveillé, R. J., Fyfe, W. S., & Longstaffe, F. J. (2000b). Unusual secondary Ca-Mg-carbonate-kerolite deposits in basaltic caves, Kauai, Hawaii. *The Journal of Geology*, 108(5), 613-621.

Léveillé, R. J., Fyfe, W. S., & Longstaffe, F. J. (2000a). Geomicrobiology of carbonate–silicate microbialites from Hawaiian basaltic sea caves. *Chemical Geology*, 169(3-4), 339-355.

Léveillé, R. J., Longstaffe, F. J., & Fyfe, W. S. (2002). Kerolite in carbonate-rich speleothems and microbial deposits from basaltic caves, Kauai, Hawaii. *Clays and Clay Minerals*, 50(4), 514-524.

Loucaides, S., Van Cappellen, P., Roubeix, V., Moriceau, B., & Ragueneau, O. (2012a). Controls on the recycling and preservation of biogenic silica from biomineralization to burial. *Silicon*, 4(1), 7-22.

Loucaides, S., Koning, E., & Van Cappellen, P. (2012b). Effect of pressure on silica solubility of diatom frustules in the oceans: Results from long-term laboratory and field incubations. *Marine Chemistry*, 136, 1-6.

Mackenzie, F. T., & Kump, L. R. (1995). Reverse weathering, clay mineral formation, and oceanic element cycles. *Science*, 270(5236), 586-586.

Melim, L. A., & Spilde, M. N. (2018). A new unified model for cave pearls: Insights from cave pearls in Carlsbad Cavern, New Mexico, USA. *Journal of Sedimentary Research*, 88(3), 344-364.

Michalopoulos, P., & Aller, R. C. (1995). Rapid clay mineral formation in Amazon delta sediments: reverse weathering and oceanic elemental cycles. *Science*, 270(5236), 614-617.

Michalopoulos, P., & Aller, R. C. (2004). Early diagenesis of biogenic silica in the Amazon delta: alteration, authigenic clay formation, and storage. *Geochimica et Cosmochimica Acta*, 68(5), 1061-1085.

Milesi, V. P., Jézéquel, D., Debure, M., Cadeau, P., Guyot, F., Sarazin, G., Claret, F., Vennin, E., Chaduteau, C., Virgone, A., Gaucher, E. C., & Ader, M. (2019). Formation of magnesium-smectite during lacustrine carbonates early diagenesis: Study case of the volcanic crater lake Dziani Dzaha (Mayotte–Indian Ocean). *Sedimentology*, 66(3), 983-1001.

Milesi, V. P., Debure, M., Marty, N. C., Capano, M., Jézéquel, D., Steefel, C., Rouchon, V., Albéric, P., Bard, E., Sarazin, G., Guyot, F., Virgone, A., Gaucher, E. C., & Ader, M. (2020). Early diagenesis of lacustrine carbonates in volcanic settings: the role of magmatic CO2 (Lake Dziani Dzaha, Mayotte, Indian Ocean). *ACS Earth and Space Chemistry*, 4(3), 363-378.

Miller, A. Z., Pereira, M. F., Calaforra, J. M., Forti, P., Dionísio, A., & Saiz-Jimenez, C. (2014). Siliceous speleothems and associated microbe-mineral interactions from Ana Heva Lava Tube in Easter Island (Chile). *Geomicrobiology Journal*, 31(3), 236-245.

Millot, G. (1970). Superficial Geochemistry and The Silicate Cycle. In: *Geology of Clays* (Ed. Springer, Berlin, Heidelberg) pp. 355-388.

Negendank, J. F. W., Emmermann, R., Krawczyk, R., Mooser, F., Tobschall, H., & Werle, D. (1985). Geological and geochemical investigations on the eastern Transmexican Volcanic Belt. *Geofísica Internacional*, 24(4), 477-575.

Nied, D., Enemark-Rasmussen, K., L'Hopital, E., Skibsted, J., & Lothenbach, B. (2016). Properties of magnesium silicate hydrates (MSH). *Cement and Concrete Research*, 79, 323-332.

Pace, A., Bourillot, R., Bouton, A., Vennin, E., Galaup, S., Bundeleva, I., Patrier, P., Dupraz, C., Thomazo, C., Sansjofre, P., Yokoyama, Y., Franceschi, M., Anguy, Y., Pigot, L., Virgone, A., & Visscher, P. T. (2016). Microbial and diagenetic steps leading to the mineralisation of Great Salt Lake microbialites. *Scientific Reports*, 6(1), 1-12.

Parkhurst, D. L., & Appelo, C. A. J. (2013). Description of input and examples for PHREEQC version 3—a computer program for speciation, batch-reaction, one-dimensional transport, and inverse geochemical calculations. *US geological survey techniques and methods*, 6(A43), 497.

Pozo, M., & Calvo, J. P. (2018). An overview of authigenic magnesian clays. *Minerals*, 8(11), 520.

Reimer, A., Landmann, G., & Kempe, S. (2009). Lake Van, eastern Anatolia, hydrochemistry and history. Aquatic Geochemistry, 15(1), 195-222.

Saghaï, A., Zivanovic, Y., Zeyen, N., Moreira, D., Benzerara, K., Deschamps, P., Bertolino, P., Rogon, M., Tavera, R., López-Archilla, A., & López-García, P. (2015). Metagenome-based diversity analyses suggest a significant contribution of non-cyanobacterial lineages to carbonate precipitation in modern microbialites. *Frontiers in microbiology*, 6, 797.

Souza-Egipsy, V., Wierzchos, J., Ascaso, C., & Nealson, K. H. (2005). Mg–silica precipitation in fossilization mechanisms of sand tufa endolithic microbial community, Mono Lake (California). *Chemical Geology*, 217(1-2), 77-87.

Stoessell, R. K. (1988). 25°C and 1 atm dissolution experiments of sepiolite and kerolite. *Geochimica et Cosmochimica Acta*, 52(2), 365-374.

Tchamabé, B. C., Carrasco-Núñez, G., Miggins, D. P., & Németh, K. (2020). Late Pleistocene to Holocene activity of Alchichica Maar volcano, eastern trans-Mexican volcanic belt. *Journal of South American Earth Sciences*, 97, 102404.

Tosca, N. J., Macdonald, F. A., Strauss, J. V., Johnston, D. T., & Knoll, A. H. (2011). Sedimentary talc in Neoproterozoic carbonate successions. *Earth and Planetary Science Letters*, 306(1-2), 11-22.

Tosca, N. J., & Masterson, A. L. (2014). Chemical controls on incipient Mg-silicate crystallization at 25 C: Implications for early and late diagenesis. *Clay Minerals*, 49(2), 165-194.

Tosca, N. J., & Wright, V. P. (2018). Diagenetic pathways linked to labile Mg-clays in lacustrine carbonate reservoirs: a model for the origin of secondary porosity in the Cretaceous pre-salt Barra Velha Formation, offshore Brazil. *Geological Society, London, Special Publications*, 435(1), 33-46.

Tosca, N. J., & Wright, V. P. (2014). The formation and diagenesis of Mg-clay minerals in lacustrine carbonate reservoirs. In: Adapted from oral presentation given at 2014 AAPG Annual Convention and Exhibition, Houston, Texas.

Truesdell, A. H., & Jones, B. F. (1974). WATEQ, a computer program for calculating chemical equilibria of natural waters. J. Res. US Geol. Surv, 2(2), 233-248.

Valdespino-Castillo, P. M., Hu, P., Merino-Ibarra, M., López-Gómez, L. M., Cerqueda-García, D., Zayas, G. D., Pi-Puig, T., Lestayo, J. A., Holman, H.-Y., & Falcón, L. I. (2018). Exploring biogeochemistry and microbial diversity of extant microbialites in Mexico and Cuba. Frontiers in microbiology, 9, 510.

Vilaclara, G., Chávez, M., Lugo, A., González, H., & Gaytán, M. (1993). Comparative description of crater-lakes basic chemistry in Puebla State, Mexico. *Internationale Vereinigung für theoretische und angewandte Limnologie: Verhandlungen*, 25(1), 435-440.

Wallmann, K., Aloisi, G., Haeckel, M., Tishchenko, P., Pavlova, G., Greinert, J., Kutterolf, S., & Eisenhauer, A. (2008). Silicate weathering in anoxic marine sediments. *Geochimica et Cosmochimica Acta*, 72(12), 2895-2918.

Weaver, C. E. (1989). *Clays, muds, and shales*. Developments in Sedimentology 44 (ed. Elsevier Science Publisher B.V., The Netherlands).

Willey, J. D. (1980). Effects of aging on silica solubility: a laboratory study. *Geochimica et Cosmochimica Acta*, 44(4), 573-578.

Wollast, R., Mackenzie, F. T., & Bricker, O. P. (1968). Experimental precipitation and genesis of sepiolite at earth-surface conditions. *American Mineralogist: Journal of Earth and Planetary Materials*, 53(9-10), 1645-1662.

Wright, V. P., & Barnett, A. J. (2015). An abiotic model for the development of textures in some South Atlantic early Cretaceous lacustrine carbonates. *Geological Society, London, Special Publications*, 418(1), 209-219.

Wright, V. P., & Barnett, A. J. (2020). The textural evolution and ghost matrices of the Cretaceous Barra Velha Formation carbonates from the Santos Basin, offshore Brazil. *Facies*, 66(1), 1-18.

Zeyen, N., Benzerara, K., Li, J., Groleau, A., Balan, E., Robert, J. L., Estève, I., Tavera, R., Moreira, D., & López-García, P. (2015). Formation of low-T hydrated silicates in modern microbialites from Mexico and implications for microbial fossilization. *Frontiers in Earth Science*, 3, 64.

Zeyen, N., Benzerara, K., Menguy, N., Brest, J., Templeton, A. S., Webb, S. M., Gérard, E., Moreira, D., López-García, P., Tavera, R., & Morin, G. (2019). Fe-bearing phases in modern lacustrine microbialites from Mexico. *Geochimica et Cosmochimica Acta*, 253, 201-230.

Zeyen, N., Benzerara, K., Beyssac, O., Daval, D., Muller, E., Thomazo, C., Tavera, R., López-García, P., Moreira, D., & Duprat, E. (2021). Integrative analysis of the mineralogical and chemical composition of modern microbialites from ten Mexican lakes: What do we learn about their formation? *Geochimica et Cosmochimica Acta*, 305, 148-184.

Supplementary Information

Diagenetic formation of stevensite by replacement of diatom frustules in the sediments of the alkaline Lake Alchichica (Mexico)

Elodie Muller[a], William Rapin[a,b], Jeanne Caumartin[a], Didier Jezequel[c], Alexis De Wever[a], Christophe Thomazo[d,e], Robin Havas[d], Purificación López-García[f], David Moreira[f], Rozaluz Tavera[g], Karim Benzerara[a]*

[a]*Sorbonne Université, Muséum National d'Histoire Naturelle, UMR CNRS 7590, Institut de Minéralogie, de Physique des Matériaux et de Cosmochimie (IMPMC), 4 Place Jussieu, 75005 Paris, France*
[b]*IRAP, CNRS UMR 5277, OMP, Université de Toulouse, France*
[c]*IPGP, CNRS UMR 7154, Université de Paris & UMR CARRTEL, INRAE-USMB, France*
[d]*UMR CNRS/uB6282 Biogéosciences, Université de Bourgogne Franche-Comté, 6 Bd Gabriel, 21000 Dijon, France*
[e]*Institut Universitaire de France, Paris, France*
[f]*Ecologie, Systématique et Evolution, CNRS, Université Paris-Saclay, AgroParisTech, Orsay, France*
[g]*Departamento de Ecología y Recursos Naturales, Universidad Nacional Autónoma de México, DF México, Mexico*

*Corresponding author: karim.benzerara@upmc.fr

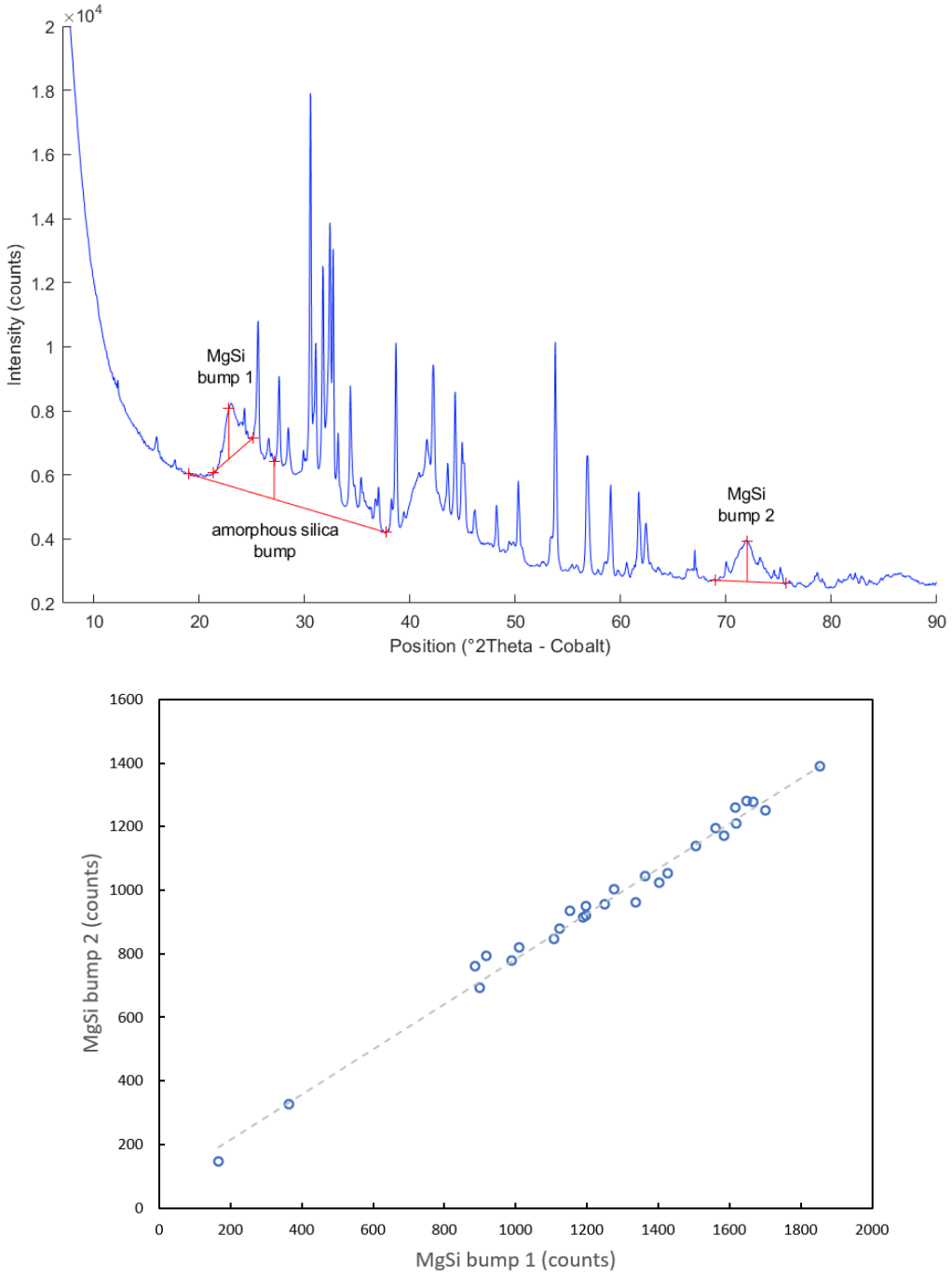

Figure S1: Poorly crystalline phases produce broad diffraction signal on the diffractograms, which intensity could be estimated. (Top) Example diffractogram (sample AL19_C2a_05) in blue with metric used to estimate "bumps" signal intensity (in red). For each signal, a linear baseline corrects for background within the diffraction windows. Then, the intensity is estimated by the signal height near the center of the window, at an angle where no interference from major diffraction peaks is found across all samples. (Bottom) Intensity of Mg-silicate bump 1 and 2 correlation for all samples highlighting the signal produced from the same low crystalline phase.

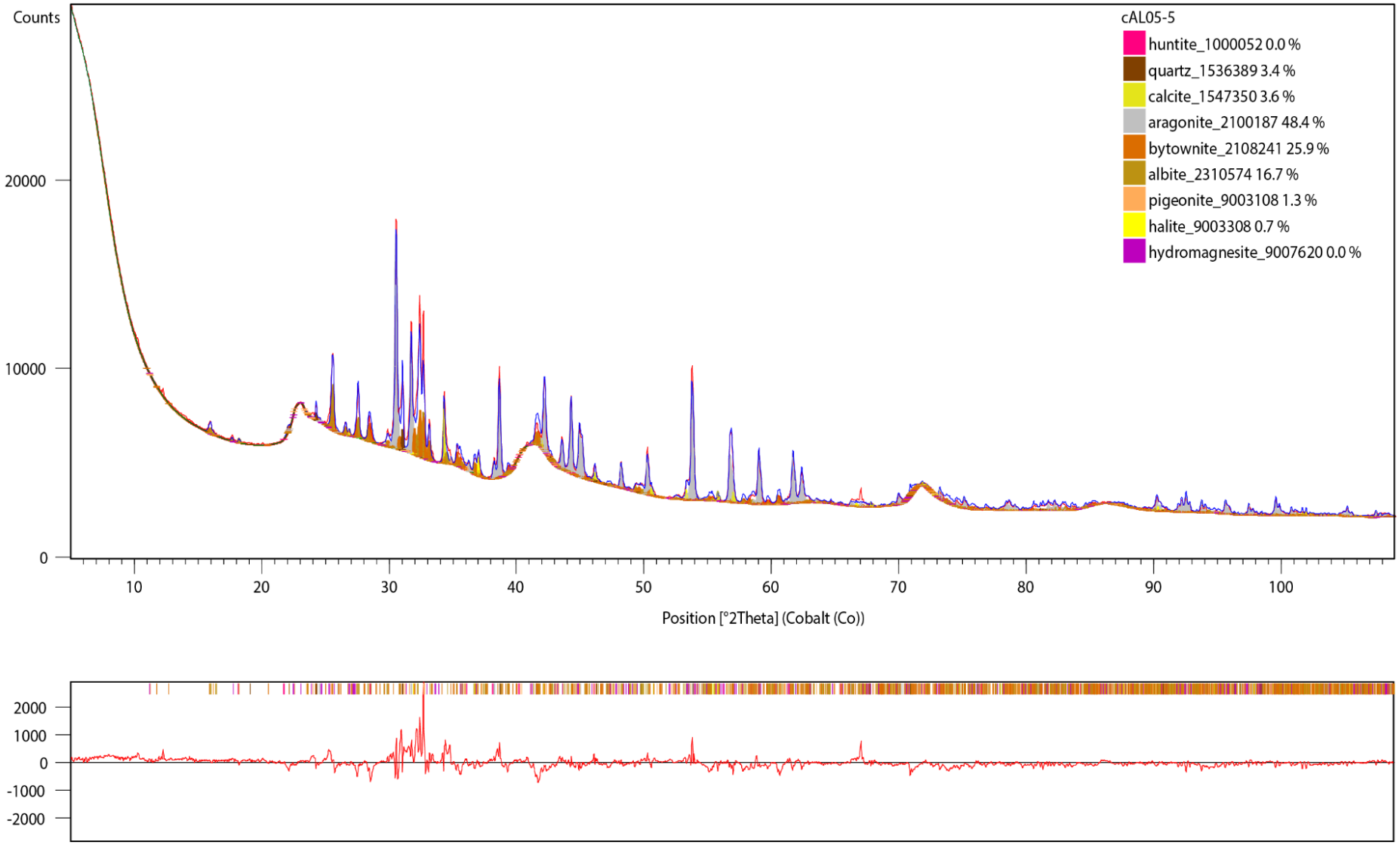
Counts
20000
10000
0
10
20
30
40
50
60
70
80
90
100
Position [°2Theta] (Cobalt (Co))
cAL05-5
huntite_1000052 0.0 %
quartz_1536389 3.4 %
calcite_1547350 3.6 %
aragonite_2100187 48.4 %
bytownite_2108241 25.9 %
albite_2310574 16.7 %
pigeonite_9003108 1.3 %
halite_9003308 0.7 %
hydromagnesite_9007620 0.0 %
2000
1000
0
-1000
-2000

Figure S2: Example Rietveld fit result (sample AL19_C2a_05) showing the actual data in red and the modeled diffractogram in blue. Each Rietveld patterns of the minerals is shown as a solid profile fill. The background signal was fit so that the contribution of X-ray low crystalline phases could be removed from peak analysis. Bottom panel shows the residual difference with fit model.

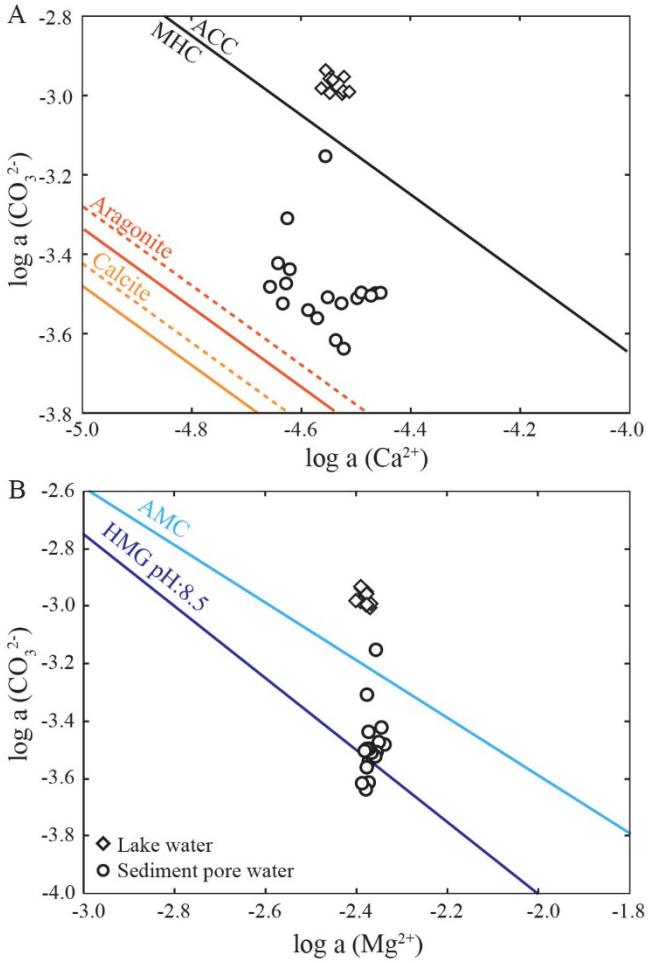

Figure S3: Solubility diagram in the a) log[a(CO_3^{2-})] – log[a(Ca^{2+})] and b) log[a(CO_3^{2-})] – log[a(Mg^{2+})] spaces. Diamonds correspond to aqueous solutions from the water column whereas circles correspond to porewaters. The solubilities of calcite and aragonite were calculated at 15°C (dashed lines) and 25°C (solid lines) using SUPCRTBL software (Zimmer et al., 2016). The solubilities of monohydrocalcite (MHC) and amorphous Mg carbonate (AMC) were defined by Fukushi and Matsumiya (2018) and the solubility of amorphous Ca carbonate (ACC) was measured by Kellermeier et al. (2014). The solubility line of hydromagnesite (HMG) was determined at 15°C using the solubility coefficient defined by Robie and Hemingway (1973) and with an average pore water pH of 8.5.

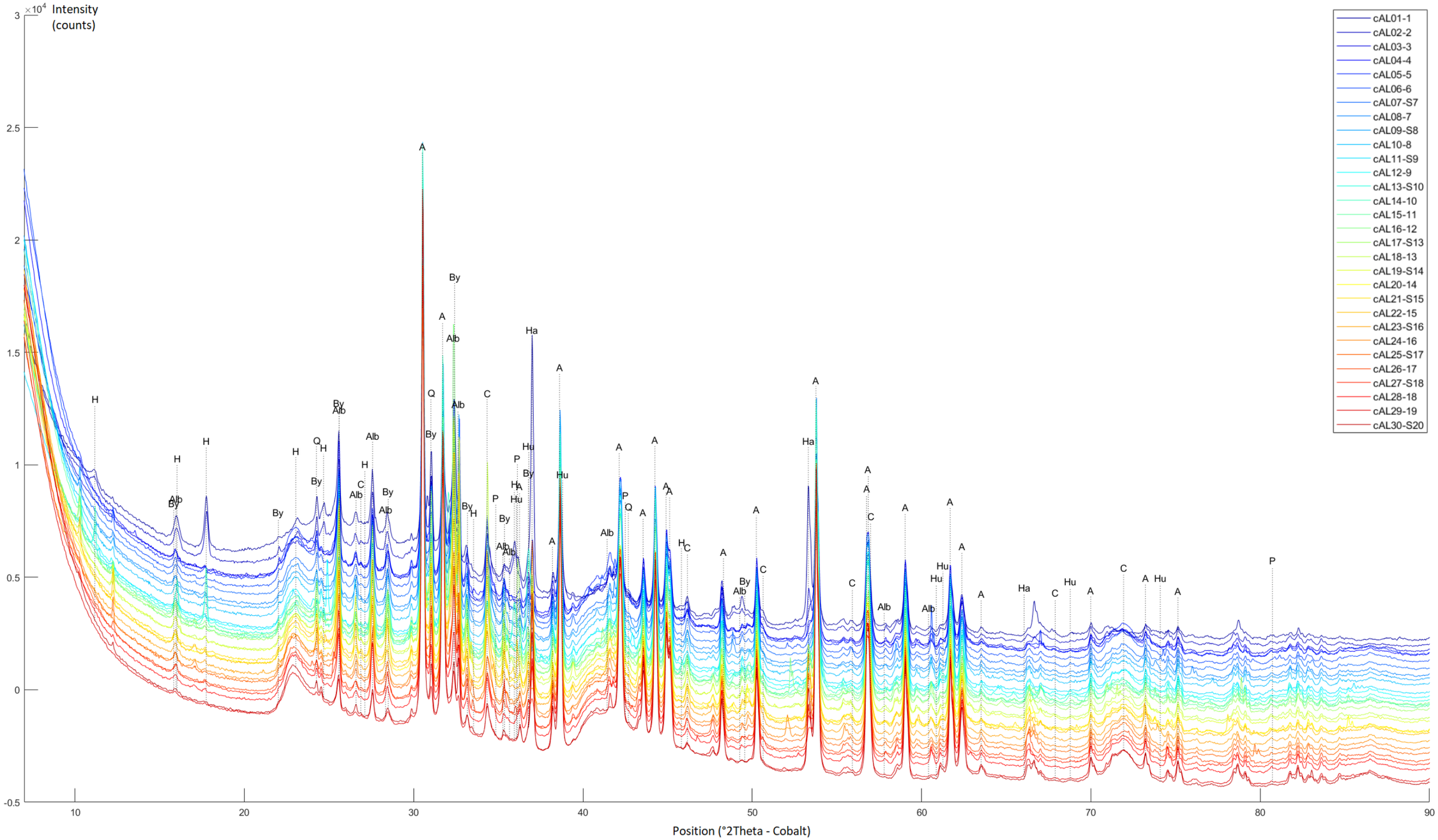

Figure S4: All diffractograms collected on samples from shallowest to deepest. Vertical annotations highlight the location of diffraction peaks from mineral species used in Rietveld fit (A: aragonite, Alb: albite, By: bytownite, H: hydromagnesite, Hu: huntite, Ha: halite, C: calcite, Q: Quartz, P: Pigeonite)

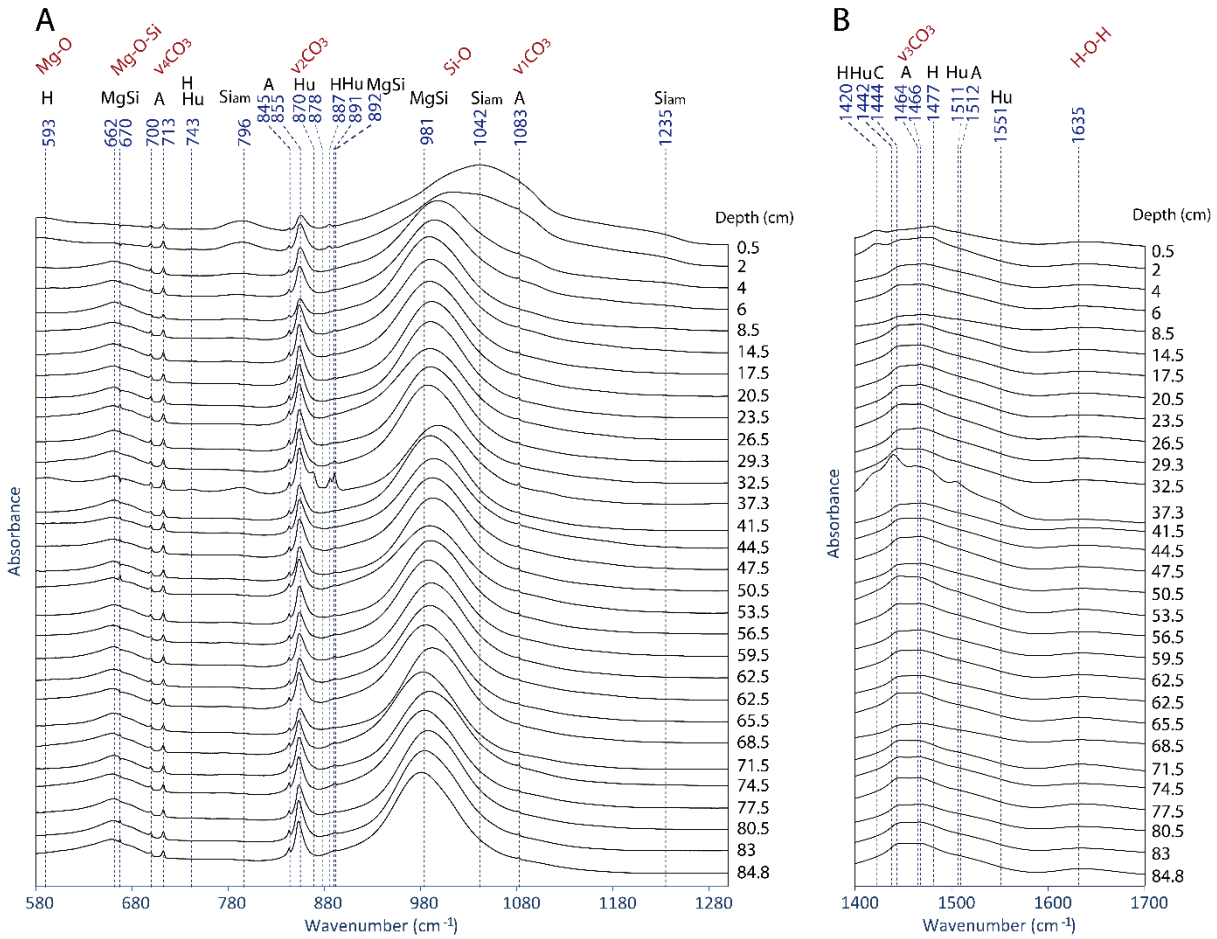

Figure S5: FTIR spectra of the Alchichica sediment cores from the shallowest to the deepest (from top to bottom). (A) Spectra in the 580 to 1280 cm^{-1} wavenumber range of Alchichica sediment cores. The dashed lines show characteristic bands of silicates [authigenic magnesium silicates (MgSi), amorphous silica (Si_{am})] and carbonates [aragonite (A), calcite (C), hydromagnesite (H), huntite (Hu)] in the samples. (B) Spectra of the same samples in the 1400 to 1700 cm^{-1} wavenumber range.

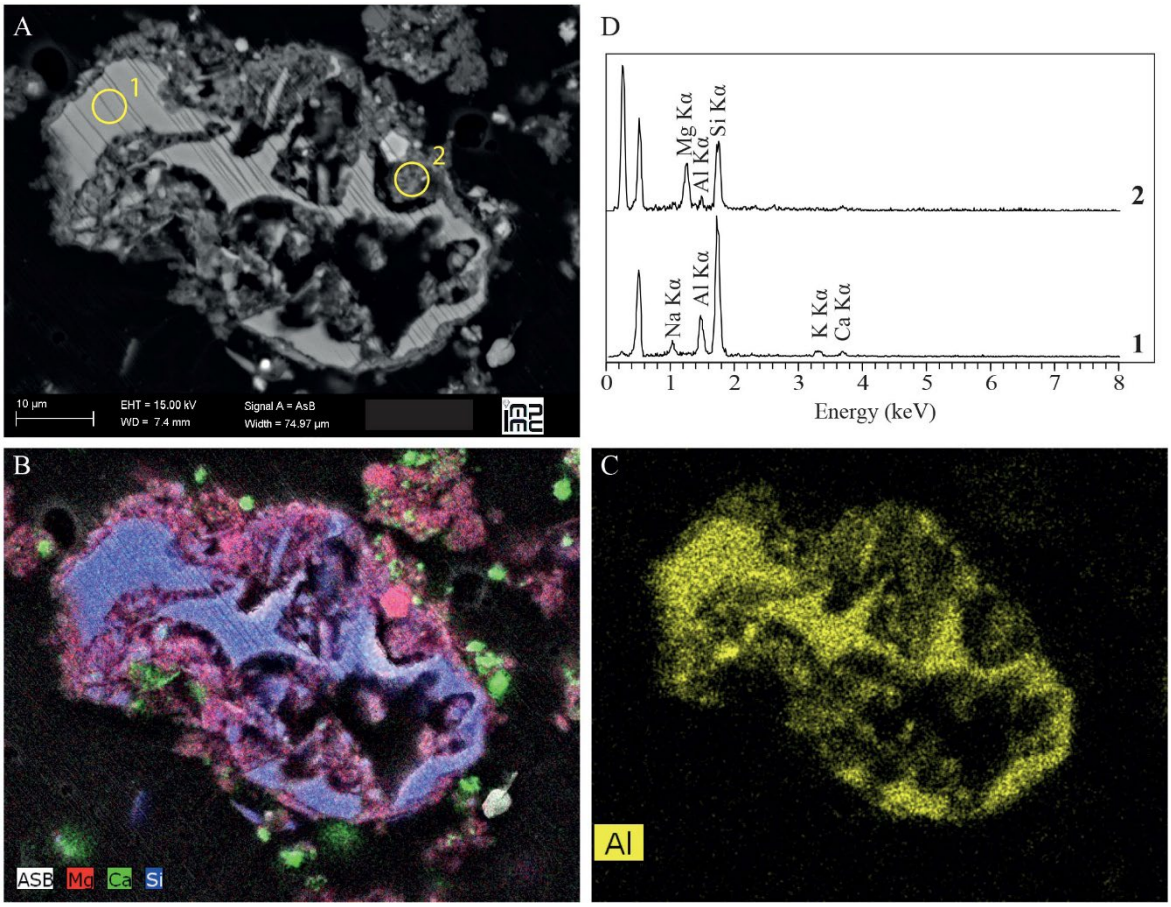

Figure S6: Mg-silicates formed around a detrital feldspar grain. (A) Backscattered electron (BSE) image, (B) corresponding EDXS maps of Mg (red), Ca (green) and Si (blue) and (C) Al (yellow). (D) EDXS spectra of the zones highlighted by yellow circles. On the chemical composition map B, aragonite appears in green, Mg-silicates in dark red and Na-Ca-K felsdpar in blue. The Mg-silicates found in the vicinity of detrital grains contain 2.41±0.85 at.% of Al in average (n=20).

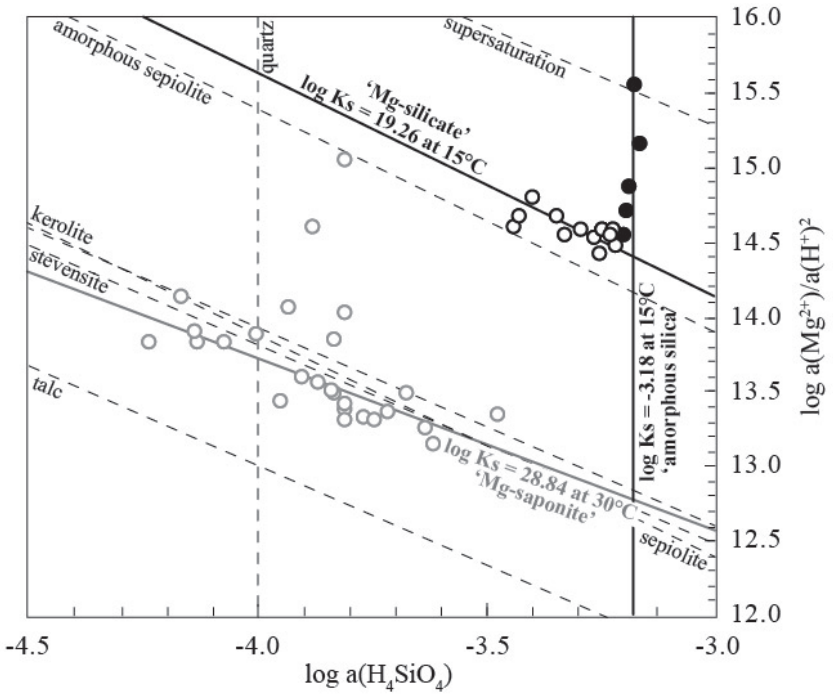

67

68 **Figure S7: Solubility diagram in the log[a(Mg^{2+})/a(H^{+})^2] – log[a(H_4SiO_4)] space**
69 **determined at 25°C.** Pore waters of Lakes Alchichica (in black) and Dziani Dzaha (Mayotte,
70 in grey) are plotted against the equilibrium solubility lines of talc (Jones and Galan 1988),
71 stevensite (Chahi et al. 1997), kerolite and sepiolite (Stoessell 1988), "amorphous sepiolite"
72 (Wollast et al. 1968), quartz and amorphous silica (Truesdell and Jones 1974) and the
73 ''supersaturation" line from Tosca et al. (2011) and Tosca and Masterson (2014). The solid
74 lines represent the solubility of Mg-saponite (in grey), amorphous silica and poorly crystalline
75 Mg-silicate (in black) deduced from the analysis of sediment porewaters respectively from
76 Dziani (Milesi et al. 2020) and Alchichica between 0 and 13 cm and between 16 and 84 cm
77 (this study).
78

79 **Table S1.** Sediment composition in wt.% estimated by Rietveld (amorphous free).

	Albite	Aragonite	Augite	Bytownite	Calcite	Halite	Huntite	Hmg	Illite	Pigeonite	Plagioclase	Quartz	Total
AL19_C2a_01	12.0	39.9	0.4	17.0	2.3	8.6	0.3	16.0	0.0	1.0	0.0	3.1	100.6
AL19_C2a_02	13.0	55.5	0.0	13.0	2.3	0.0	0.3	12.2	0.0	0.7	0.0	2.7	99.6
AL19_C2a_03	15.0	61.1	0.0	15.0	2.2	2.5	0.6	0.0	0.0	0.6	0.0	3.5	100.4
AL19_C2a_04	12.0	60.7	0.0	19.0	2.6	0.1	0.9	0.0	0.0	0.8	0.0	3.0	99.1
AL19_C2a_05	17.0	48.4	0.0	26.0	3.6	0.7	0.0	0.0	0.0	1.3	0.0	3.4	100.3
AL19_C2a_06	15.0	55.1	0.0	22.0	3.2	0.2	0.2	0.0	0.0	1.3	0.0	2.8	99.8
AL19_C2a_S7	17.0	55.4	0.0	18.0	2.6	0.2	0.6	0.9	0.2	1.5	0.0	2.9	99.3
AL19_C2a_07	12.0	60.7	0.0	19.0	2.7	0.1	0.0	0.7	0.8	1.4	0.0	2.1	99.5
AL19_C2a_S8	14.0	57.8	0.1	20.0	2.4	0.1	0.5	0.2	0.3	1.3	0.0	3.4	100.1
AL19_C2a_S9	12.0	63.7	0.3	17.0	1.8	0.0	0.0	0.2	0.0	2.1	0.1	2.7	99.9
AL19_C2a_S10	12.0	49.5	0.3	13.0	1.7	0.1	11.6	8.7	0.0	1.3	0.0	2.0	100.2
AL19_C2a_10	15.0	47.1	0.0	14.0	1.5	0.2	10.6	7.3	0.2	1.0	0.0	2.1	99.0
AL19_C2a_11	18.0	56.6	0.1	16.0	2.0	1.4	0.2	0.8	0.8	1.4	0.2	2.6	100.1
AL19_C2b_12	17.0	43.8	0.1	27.0	3.5	2.0	0.2	0.6	0.1	1.6	0.2	3.4	99.4
AL19_C2b_S13	16.0	47.5	0.3	23.0	3.3	0.5	0.5	0.8	0.7	3.6	0.2	4.0	100.4
AL19_C2b_13	15.0	51.2	0.0	18.0	7.2	2.8	0.5	0.5	0.2	1.2	0.1	3.1	99.8
AL19_C2b_S14	15.0	50.9	0.0	26.0	3.3	0.1	0.0	0.7	0.0	1.3	0.1	3.0	100.4
AL19_C2b_14	9.0	59.6	0.4	19.0	2.6	2.7	1.5	0.7	0.3	1.1	0.1	2.5	99.6
AL19_C2b_S15	10.0	54.8	0.1	26.0	3.1	0.2	0.4	1.1	0.0	1.4	0.0	3.0	100.1
AL19_C2b_15	17.0	47.5	0.0	22.0	5.7	1.9	0.6	0.5	0.0	2.3	0.0	2.7	100.2
AL19_C2b_S16	17.0	58.2	0.0	17.0	2.8	0.2	0.4	0.3	0.1	1.1	0.0	2.8	99.9
AL19_C2b_16	13.0	63.1	0.0	12.0	1.7	4.3	1.1	0.3	0.8	0.7	0.0	2.1	99.2
AL19_C2b_S17	14.0	57.0	0.3	19.0	1.8	2.7	0.7	0.5	0.5	1.0	0.0	2.1	99.6
AL19_C2b_17	9.0	68.1	0.0	15.0	1.5	1.3	0.9	0.6	0.4	0.5	0.0	2.5	99.8
AL19_C2b_S18	8.3	35.1	0.0	52.0	0.9	0.4	0.3	0.4	0.4	0.5	0.0	1.4	99.7
AL19_C2b_18	12.0	70.1	0.0	10.0	1.9	1.8	0.9	0.5	0.4	1.3	0.0	2.0	100.8
AL19_C2b_19	6.0	79.8	0.0	8.0	1.3	3.0	1.4	0.0	0.0	0.2	0.0	0.9	100.7
AL19_C2b_S20	11.0	76.0	0.1	2.0	1.0	4.0	1.0	0.0	1.0	1.0	0.0	2.0	99.1

80

Table S2. Stoichiometry of the mineral phases estimated by EDXS.

	Si/O	Mg/O	Ca/O	Fe/O	Al/O	Na/O	Formula
Bytownite (n=5)	0.37		0.07		0.22	0.07	$(Ca_{0.5}Na_{0.5})(Al(Al_{0.5}Si_{0.5})Si_2O_8$
Albite (n=5)	0.38				0.15	0.13	$NaAlSi_3O_8$
Pyroxene (n=7)	0.29	0.13	0.13	0.03			$(Ca_{0.45}Mg_{0.45}Fe_{0.1})Si_2O_6$
Olivine (n=12)	0.19	0.31	0.02	0.08			$(Fe_{0.3}Mg_{0.7})_2SiO_4$
Quartz (n=5)	0.50						SiO_2

Table S3. Method for quantification of mineral phases.

Mineral	Chemical Formula	Calculation***
Feldspars*	$Ca_{0.25}Na_{0.25}Al_{1.25}Si_{2.75}O_8$	Felds = [Al] / 1.25
Aragonite	$CaCO_3$	A = [Ca] – (Felds x 0.25) – (Mg_{Carb} x 0.6)
Mg-silicates	$Mg_3Si_4O_{10}(OH)_2$	MgSi = [Mg] / 3 or ([Si] – Felds x 2.75) / 4**
Hydromagnesite	$Mg_5(CO_3)_4(OH)_2\ 4H_2O$	H = [Mg] / 5
Amorphous silica	SiO_2	Si_{am} = [Si] – (Felds x 2.75) – (MgSi x 4)
Mg-carbonates**	$Ca_{0.6}Mg_{3.8}(CO_3)_4(OH)_{0.8}(H_2O)_{1.6}$	Mg_{Carb} = ([Mg] – MgSi x 3) / 3.8

* Mix 50/50 Albite-Bytownite based on XRD results (at all depths)

** Mix 40/60 Hydromagnesite-Huntite based on XRD results (at 30.5-40 cm depth)

*** [X] are the concentrations in mol.% measured by ICP-AES

References

Zimmer, K., Zhang, Y.L., Lu, P., Chen, Y.Y., Zhang, G.R., Dalkilic, M. and Zhu, C. (2016) SUPCRTBL: A revised and extended thermodynamic dataset and software package of SUPCRT92. Computer and Geosciences 90:97-111.